Article

Molecular basis of receptor binding and antibody neutralization of Omicron

https://doi.org/10.1038/s41586-022-04581-9

Received: 11 January 2022

Accepted: 24 February 2022

Published online: 28 February 2022

Check for updates

Qin Hong[1,2,4], Wenyu Han[1,2,4], Jiawei Li[1,2,4], Shiqi Xu[3,4], Yifan Wang[1,2,4], Cong Xu[1], Zuyang Li[1,2], Yanxing Wang[1]✉, Chao Zhang[3]✉, Zhong Huang[3]✉ & Yao Cong[1,2]✉

The SARS-CoV-2 Omicron variant exhibits striking immune evasion and is spreading rapidly worldwide. Understanding the structural basis of the high transmissibility and enhanced immune evasion of Omicron is of high importance. Here, using cryo-electron microscopy, we present both the closed and the open states of the Omicron spike (S) protein, which appear more compact than the counterparts of the G614 strain[1], potentially related to enhanced inter-protomer and S1–S2 interactions induced by Omicron residue substitution. The closed state showing dominant population may indicate a conformational masking mechanism for the immune evasion of Omicron. Moreover, we captured three states for the Omicron S–ACE2 complex, revealing that the substitutions on the Omicron RBM result in new salt bridges and hydrogen bonds, more favourable electrostatic surface properties, and an overall strengthened S–ACE2 interaction, in line with the observed higher ACE2 affinity of Omicron S than of G614. Furthermore, we determined the structures of Omicron S in complex with the Fab of S3H3, an antibody that is able to cross-neutralize major variants of concern including Omicron, elucidating the structural basis for S3H3-mediated broad-spectrum neutralization. Our findings shed light on the receptor engagement and antibody neutralization or evasion of Omicron and may also inform the design of broadly effective vaccines against SARS-CoV-2.

Severe acute respiratory syndrome coronavirus 2 (SARS-CoV-2) has undergone considerable evolution since its initial discovery, leading to the emergence of several variants of concern (VOCs) including Alpha[2–6], Beta[5–10], Gamma[11] and Delta[12,13]. These variants that have multiple mutations on their S protein show enhanced transmissibility and resistance to antibody neutralization[13]. Recently, a new variant named Omicron (B.1.1.529), which was first reported in South Africa in November 2021, was classified as the fifth VOC by the World Health Organization (WHO)[14]. Omicron bears 37 mutations in its S protein relative to the original SARS-CoV-2 strain[15,16]. As a consequence, Omicron has been observed to extensively escape neutralization by previously developed neutralizing monoclonal antibodies (mAbs) or sera from vaccinated or convalescent individuals[15,17–22]. Among all of the Omicron S mutations, 15 are present in the receptor-binding domain (RBD) that mediates binding of the virus to its host cell receptor, angiotensin-converting enzyme 2 (ACE2), which is also a major target for neutralizing antibodies[23–27]. However, Omicron still uses ACE2 as its entry receptor[22]. Moreover, the Omicron S appears to have an increased binding affinity to ACE2 relative to the wild-type (WT) S[15,16,28].

The high transmissibility and greatly enhanced resistance to antibody neutralization observed for Omicron makes this VOC particularly threatening. Therefore, further understanding of the nature of Omicron is of substantial importance and may help in developing countermeasures against this VOC. To address this from a structural aspect of how Omicron binds to the ACE2 receptor and how it recognizes or evades neutralizing antibodies raised to the original virus, here we performed cryo-electron microscopy (cryo-EM) analyses on the Omicron S trimer and its complexes with ACE2 or with neutralizing mAbs.

Closed and open states of Omicron S protein

We prepared a prefusion-stabilized trimeric S protein of the SARS-CoV-2 Omicron variant (Extended Data Fig. 1) and determined its cryo-EM structures. Three cryo-EM maps, including an all RBD down conformation (termed Omicron S-close), an RBD-1 up open conformation (termed Omicron S-open), and an RBD-1 up while RBD-3 disordered open conformation (termed Omicron S-open-2), were determined at 3.08, 3.40 and 3.41 Å resolution, respectively (Fig. 1a, b, Extended Data Fig. 2a–e, Extended Data Table 1). For the Omicron S-close state, the three protomers are well resolved and they display similar conformation with their RBDs in the down position (Fig. 1c, Extended Data Fig. 2d). The Omicron S-close appears more twisted and compact in the RBDs than the G614 S-close structure[1] (Fig. 1d). In addition, in the Omicron S-open state, the RBDs are slightly more twisted and compact than that of the G614 S-open state[1] (Fig. 1e). There is no linoleic acid (termed LA) in the Omicron S-close, S-open and S-open-2 maps, and LA has been suggested to lead to more compact RBDs[29]. Thus, the Omicron S trimer is more compact than that of G614, and this is not caused by binding of LA. Moreover, in the

[1]State Key Laboratory of Molecular Biology, National Center for Protein Science Shanghai, Shanghai Institute of Biochemistry and Cell Biology, Center for Excellence in Molecular Cell Science, Chinese Academy of Sciences, Shanghai, China. [2]University of Chinese Academy of Sciences, Beijing, China. [3]CAS Key Laboratory of Molecular Virology and Immunology, Institut Pasteur of Shanghai, Chinese Academy of Sciences, University of Chinese Academy of Sciences, Shanghai, China. [4]These authors contributed equally: Qin Hong, Wenyu Han, Jiawei Li, Shiqi Xu, Yifan Wang. ✉e-mail: yxwang@sibcb.ac.cn; chaozhang@ips.ac.cn; huangzhong@ips.ac.cn; cong@sibcb.ac.cn

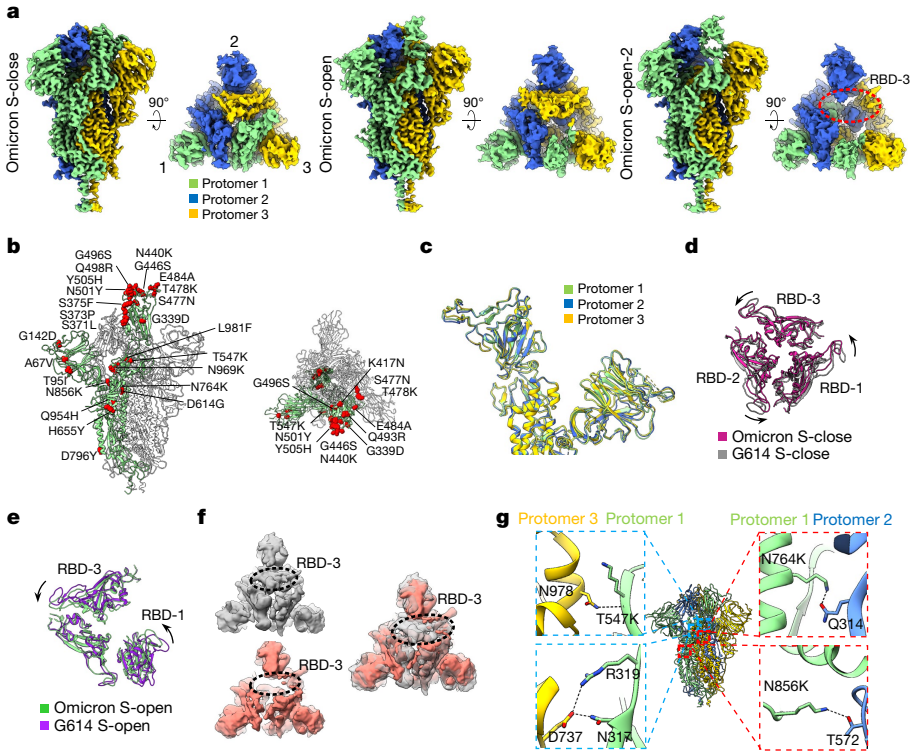

Fig. 1 | Cryo-EM structures of the SARS-CoV-2 Omicron S trimer. a, Cryo-EM maps of the Omicron S-close, S-open and S-open-2 states. Protomers 1, 2 and 3 are shown in light green, royal blue and gold, respectively; this colour scheme is followed throughout. In S-open-2, the mostly disordered RBD-3 is indicated by a red dotted ellipsoid. **b**, Atomic model of the Omicron S-open, with mutations labelled and indicated by a red sphere. **c**, Side view of the overlaid protomers of the Omicron S-close. **d**, Top view of the overlaid RBDs of the Omicron S-close (violet red) and the G614 S-close (PDB: 7KRQ; dark grey), indicating a twist of the Omicron S-close relative to that of G614. **e**, Top view of the overlaid RBDs of the Omicron S-open (light green) and the G614 S-open (PDB: 7KRR; purple), indicating a twist of the Omicron S-open relative to that of G614. **f**, One representative 3D variability analysis motion of the Omicron S. The two left maps illustrate the top view of two extremes in the motion, with the RBD-3 indicated by a black dotted ellipsoid; the top view of the overlaid two extreme maps is shown on the right. **g**, Newly formed hydrogen bonds (black dashed line) in the interfaces of protomer 1–protomer 3 (blue dashed line box) and protomer 1–protomer 2 (red dashed line box) of the S-close state (see also Extended Data Fig. 2f).

Omicron S-open-2 map, the RBD-3 density appears mostly disordered, indicating an extremely dynamic nature of RBD-3 (Fig. 1a). Further 3D variability analysis[30] on the Omicron S trimer dataset revealed an intrinsic rising up motion of RBD-1, which could alter the original RBD-1–RBD-3 contact and destabilize RBD-3, making it extremely dynamic and may transiently rise up (Fig. 1f, Supplementary Video 1).

The population distribution of the Omicron closed and open states (S-open and S-open-2) is about 60.8% and 39.2%, respectively (Extended Data Fig. 2a), displaying a considerable population shift to the closed state than that of the Beta and Kappa S protein (both around 50.0:50.0% open-transition ratio) or that of the Delta S protein (75.3:24.7% open-transition ratio) from our recent studiues[10,31], with these S structures obtained in the same sample preparation and data processing schemes. Thus, the Omicron S trimer appears more prone to the closed state and potentially stabilized relative to the counterparts of the Delta, Kappa, Beta or G614 variants. The population distribution of the closed and open states of these S trimers varies among different studies, which could potentially be due to subtle difference in the chemical condition used by different research groups[32–35]. Inspection of the protomer interaction interface of Omicron S-close revealed new hydrogen bond interactions induced by the unique Omicron substitutions in the SD1 and S2 regions (Fig. 1g, Extended Data Fig. 2f, Extended Data Table 2). Specifically, T547K from the SD1 subdomain of protomer 1 forms a new hydrogen bond with N978 from the S2 subunit of protomer 3, potentially enhancing the S1–S2 interaction between the two protomers; N856K or N764K from protomer 1 can form hydrogen bonds with T572 or Q314 from protomer 2, respectively. We also observed multiple new such interactions between N317 or R319 of protomer 1 and D737 of protomer 3 (Fig. 1g, Extended Data Fig. 2f). The SD1 and SD2 of S1 is the hinge for RBD upward rotation[31,35–38], and disturbing the SD1–S2 interface could destabilize the interface and increase S1 mobility[36]. Collectively, these extra hydrogen bonds mainly induced by Omicron substitutions contribute greatly to strengthen the inter-protomer and S1–S2 interactions, markedly stabilizing the Omicron S trimer and inhibiting its transformation towards the fusion-prone open state and subsequent shielding of S1.

Structure of enhanced S–ACE2 interaction

Compared with the WT strain, Omicron bears 15 mutations in the RBD region, nine of which are located in the receptor-binding motif (RBM)[15]. We assessed whether these mutations affect the human ACE2 receptor-binding ability of the Omicron S trimer by performing biolayer interferometry assay. We found that the ACE2-binding affinity of the Omicron S (dissociation constant (K_d) = 80 nM) is comparable to that of the Delta S (K_d = 88 nM) but is about threefold higher than that of the G614 S (K_d = 237 nM; Fig. 2a), consistent with other recent reports[15,16,28].

Next, we carried out cryo-EM analysis on the Omicron S in complex with the human ACE2 peptidase domain (Extended Data Fig. 3a). We obtained three cryo-EM maps of the S trimer engaged with ACE2, including a one RBD-up state (termed Omicron S–ACE2-C1), a two RBD-up state (termed Omicron S–ACE2-C2) and an all three RBD-up state (termed Omicron S–ACE2-C3) at 3.69, 3.70 and 4.04 Å resolution, respectively (Fig. 2b, Extended Data Fig. 4, Extended Data Table 1). The population distribution among Omicron S–ACE2-C1, S–ACE2-C2 and S–ACE2-C3 is about 43.9%, 41.2% and 14.9%, respectively (Extended Data Fig. 3b), displaying an obvious higher one RBD-up C1 population

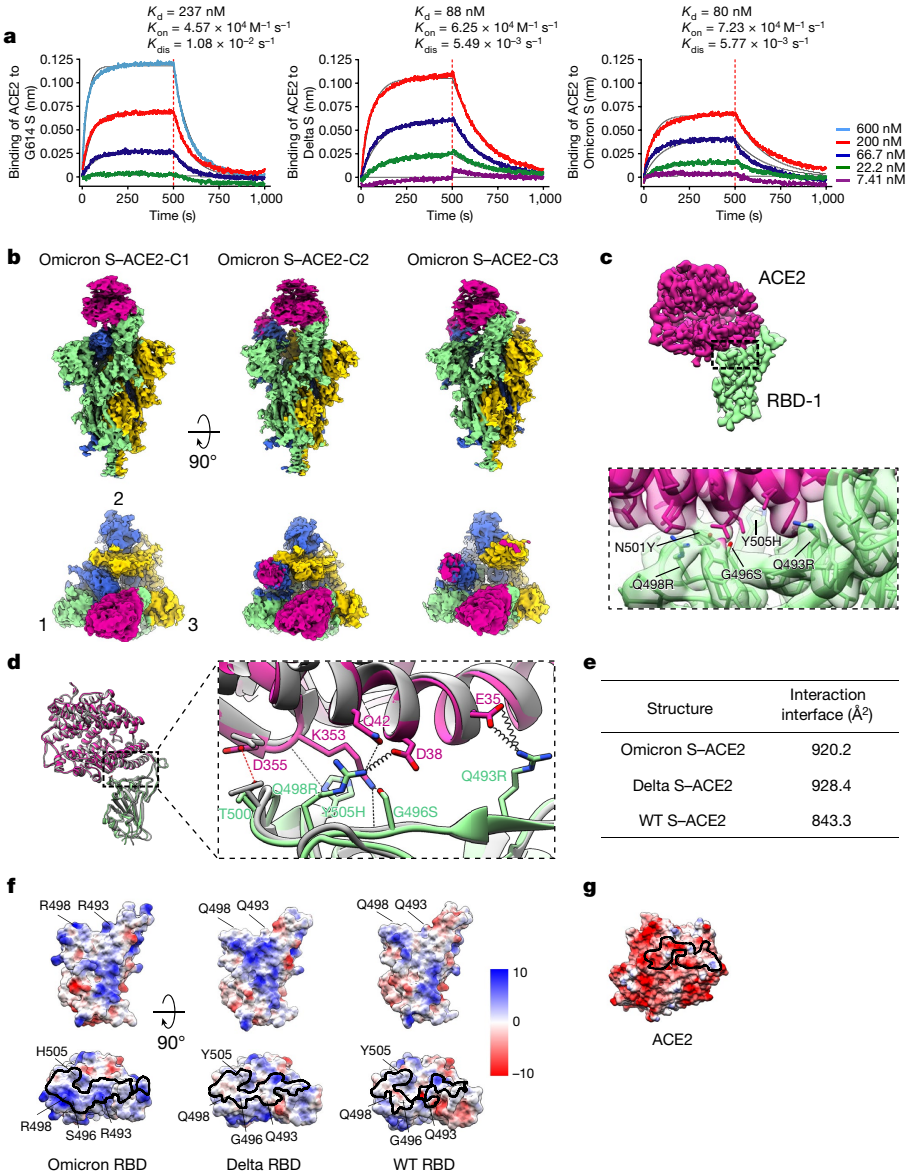

Fig. 2 | Structural basis of the enhanced Omicron S–ACE2 interaction. **a**, Measurement of the binding affinity between the ACE2 monomer and the S trimer of the G614 (left), Delta (middle) and Omicron (right) variants using biolayer interferometry. Biotinylated S trimers were loaded onto streptavidin sensors and were then allowed to interact with different concentrations of ACE2 (shown on the right). Raw sensorgrams and fitting curves are shown in colour and grey, respectively. Association and dissociation phases are divided by the red dashed lines. K_{dis}, dissociation rate; K_{on}, 'on-rate'. **b**, Cryo-EM maps of the Omicron S–ACE2 complex in three distinct conformational states. In the S–ACE2-C2 and S–ACE2-C3 maps, the density of RBD-2-associated or RBD-3-associated ACE2 appears weaker than that of the stably associated ACE2 on RBD-1 (see also Extended Data Fig. 3c). ACE2 is shown in violet red. This colour scheme is followed throughout. **c**, Density map of the focus-refined Omicron RBD-1–ACE2 and the zoomed-in view of the RBD–ACE2 interaction interface, showing the side chain densities of Q493R, G496S, Q498R, N501Y and Y505H on the RBM. **d**, The substituted residues R493, S496, R498 and H505 of the Omicron RBM form new interactions with E35, D38, Q42 and K353 of ACE2 (the spring represents the salt bridge, and the black dashed line represents the hydrogen bond) relative to that in the WT RBD–ACE2 (PDB: 6M0J; dark grey). A newly formed hydrogen bond without substitution is shown by a red dashed line. **e**, Interaction interface areas between ACE2 and the RBD of Omicron, Delta (PDB: 7W9I) and WT (PDB: 6M0J), analysed using PISA. **f**, The electrostatic surface properties of Omicron, Delta (PDB: 7W9I) and WT (PDB: 6M0J) RBDs, with the mutated residues indicated. The black outlines depict the footprint of ACE2 on the RBD. **g**, The electrostatic surface property of ACE2, with residues in proximity to RBD-1 (less than 4 Å) indicated (related to Extended Data Table 3).

(43.9%) than that of the Beta, Kappa or Delta variants (C1 population ranges from 8.3% to 14.1%) observed in our recent studies[10,31], with these S–ACE2 structures obtained in the same sample preparation and processing schemes. Together, the Omicron S trimer exhibits less ability to transform to the more RBD-up C2 or C3 states in the presence of ACE2 than that of the Beta, Kappa and Delta variants.

We further focus-refined the stably associated Omicron RBD-1–ACE2 region and obtained a 3.67 Å resolution structure (Fig. 2c, Extended Data Figs. 3, 4), which revealed many new interactions between the RBM substitutions and ACE2 compared with that of the WT RBD–ACE2 (ref. [26]). Specifically, the RBM Q493R and Q498R result in three new salt bridges with the ACE2 E35 and D38, respectively; the RBM G496S and Y505H with ACE2 K353, the RBM Q498R with ACE2 Q42, and the RBM S477N with ACE2 Q19 also form new hydrogen bonds, respectively (Fig. 2d, Extended Data Table 3), generally in line with recent studies[16,28,39–42]. Moreover, we observed an extra hydrogen bond between RBM T500 and

a

mAb	IC_{50} value (ng ml^{-1})			IC_{50} value (nM)			IC_{50} fold change in variant PV neutralization (relative to WT)	
	WT	Delta	Omicron	WT	Delta	Omicron	Delta	Omicron
3C1	286.7	231.1	>10,000	1.911	1.541	>66.667	1.2	<–34.9
2H2	9.1	6.3	30.4	0.061	0.042	0.203	1.4	–3.3
8D3	6.5	6.4	>10,000	0.043	0.043	>66.667	1.0	<–1,538
S5D2	8.2	734.6	>10,000	0.055	4.897	>66.667	–89.6	<–1,220
S3H3	82.2	39.3	53.3	0.548	0.262	0.355	2.1	1.5

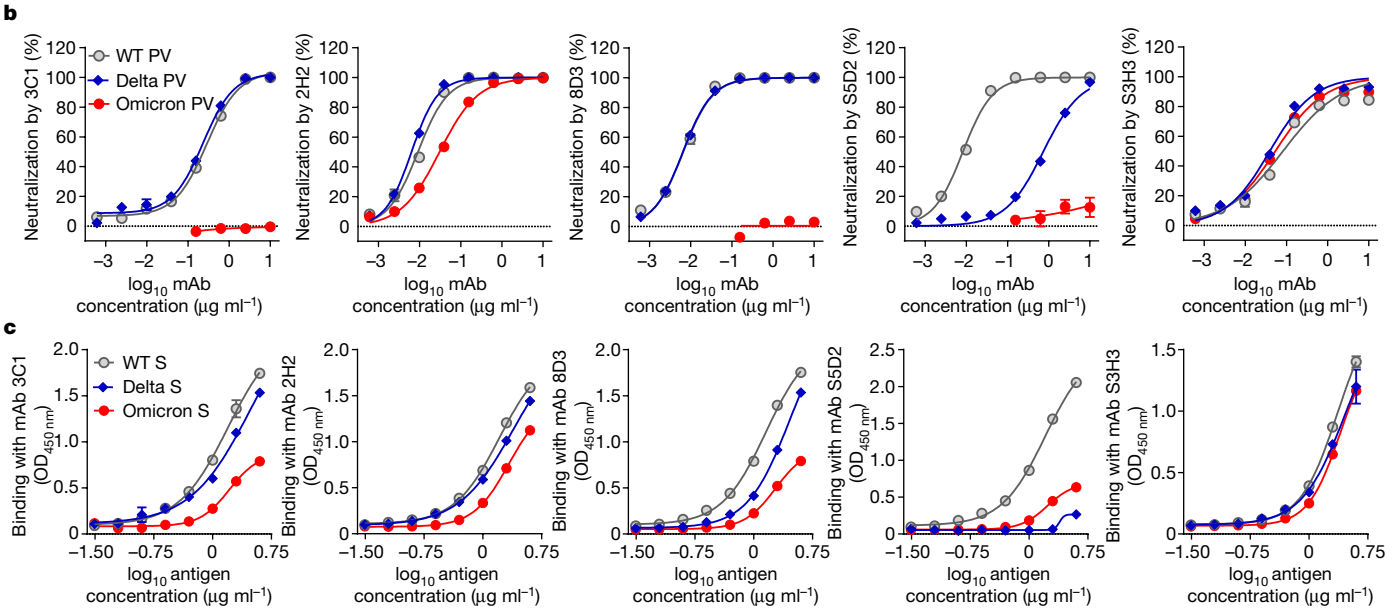

Fig. 3 | Neutralization and binding activities of the mAbs against Omicron and Delta variants. The mAbs were raised to WT RBD or S trimer proteins. **a**, Neutralization IC_{50} values and fold changes in neutralization potency for the Delta and Omicron variant pseudoviruses (PVs) compared to the WT pseudovirus. A minus sign (–) denotes decrease. The yellow highlighting indicates a more than tenfold decrease; the red highlighting denotes a more than 1,000-fold decrease. **b**, Neutralization of the mAbs towards WT, Delta and Omicron pseudoviruses. All mAbs were fourfold serially diluted. Data are expressed as mean ± s.e.m. of four replicate wells. The horizontal black dotted lines indicate 0% neutralization. **c**, Binding activities of the mAbs to recombinant S trimers of the WT, Delta and Omicron strains were tested by ELISA. Serially diluted S trimer proteins were coated onto the ELISA wells. Data are mean ± s.d. of triplicate wells. Neutralization and ELISA data are representative of two independent experiments with similar results.

ACE2 D355 (Fig. 2d). Our previous study showed that Y505A obviously decreased the binding affinity of ACE2 (ref. [35]), thus the Omicron Y505H substitution may maintain or even enhance ACE2 binding. Meanwhile, the K417N substitution, which occurred in Omicron as well as in Beta and Delta, is known to markedly reduce the binding of ACE2 through abolishing multiple salt bridges and/or hydrogen bonds with ACE2 D30 (refs. [26,43,44]). Together, these newly formed RBM–ACE2 interactions may compensate for the loss of some of the original RBM–ACE2 interactions due to the residue changes introduced into the Omicron RBM.

Further inspection of the surface property showed that the substitutions in RBM, especially Q493R, G496S, Q498R and Y505H, render the substituted site within the ACE2 interaction footprint more positively charged, which could strengthen the interaction of RBM with the overall negatively charged ACE2 in the interaction interface (Fig. 2f, g). Corroborating this, the Omicron RBD–ACE2 interaction area (920.2 Å^2) was enlarged compared to that of the WT (843.3 Å^2), whereas it was comparable to that of the Delta RBD–ACE2 (928.4 Å^2)[31] (Fig. 2e). This is also in agreement with our biolayer interferometry data showing that the ACE2-binding affinity of the Omicron S is similar to that of the Delta S but is higher than that of the G614 S (Fig. 2a).

Omicron sensitivity to neutralizing mAbs

We compared five previously generated mAbs—2H2, 3C1, 8D3, S5D2 and S3H3 (refs. [45,46])—for neutralization of the WT (Wuhan-Hu-1 strain), Delta or Omicron pseudoviruses (Fig. 3a, b). The half-maximal inhibitory concentration (IC_{50}) values of the mAbs 3C1, 2H2, 8D3 and S3H3 against Delta were comparable (less than 2.5-fold variation) to the corresponding ones against WT, whereas S5D2 was still neutralizing to Delta (IC_{50} = 734.6 ng ml^{-1}) but was about 90-fold less potent. In Omicron neutralization tests, 3C1, 8D3 and S5D2 lost neutralization activity (IC_{50} > 10 μg ml^{-1}). However, 2H2 and S3H3 remained highly effective against Omicron with IC_{50}s being 30.4 and 53.3 ng ml^{-1}, respectively, despite observing a 3.3-fold increase (relative to the WT) in the IC_{50} value for 2H2. Thus, 2H2 and S3H3 are two potent neutralizing mAbs against Omicron.

We then compared the binding ability of the five mAbs to the WT, Delta and Omicron S proteins by ELISA (Fig. 3c). For mAb S5D2, its binding to the Delta S and to the Omicron S was nearly abolished; for mAbs 3C1 and 8D3, their reactivity profile with the Delta S closely resembled that towards the WT S but their binding to the Omicron S was substantially reduced; for mAb 2H2, its binding curve to the Omicron S was similar to those towards the WT S and the Delta S, despite the binding efficiency to the Omicron S being slightly lower; meanwhile, mAb S3H3 produced nearly identical binding curves to the three S proteins. Overall, the antigen-binding ability of the mAbs was in good agreement with their neutralization potency towards specific variant pseudovirus (Fig. 3). Collectively, the above data showed that Omicron remains sensitive to binding and neutralization by the mAbs 2H2 and S3H3, whereas it displays resistance to 3C1, 8D3 and S5D2.

Structure of the Omicron S–S3H3 complex

The mAb S3H3 is a unique neutralizing antibody that binds to the SD1 region of the WT S[46]. Our cryo-EM study revealed two states of the

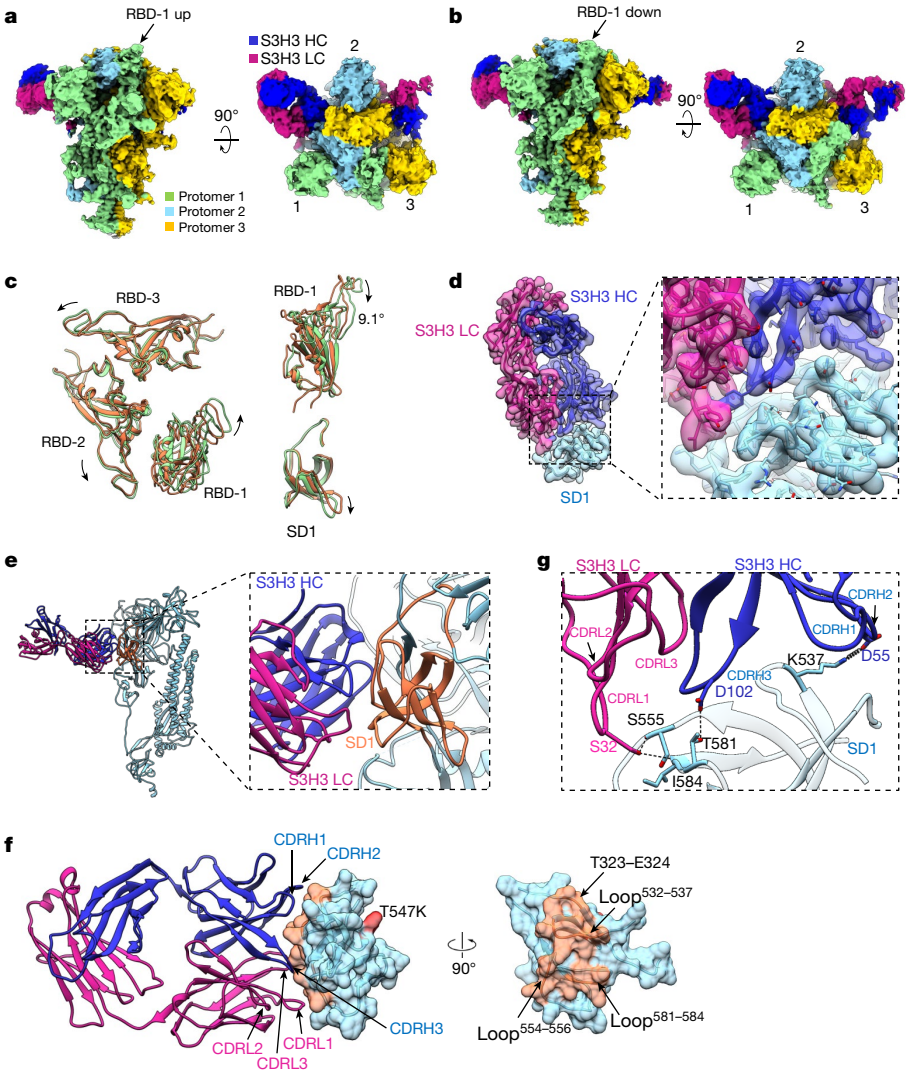

Fig. 4 | Cryo-EM analyses on the Omicron S–S3H3 Fab complex. a, **b**, Side and top views of the cryo-EM map of the Omicron S-open–S3H3 (**a**) and S-close–S3H3 complex (**b**), with the heavy chain (HC) and light chain (LC) of S3H3 Fab in medium blue and violet red, respectively. This colour scheme is followed throughout this figure. **c**, Conformational comparison between Omicron S-open–S3H3 (light green) and Omicron S-open (orange), indicating a slight twist of the RBDs of S-open–S3H3 and the downward rotations of RBD-1 (up to 9.1°) and SD1. **d**, Model map fitting of the focus-refined Omicron SD1–S3H3 structure, and the zoomed-in view of the Omicron SD1–S3H3 interaction interface. The side chain densities at the interface were well resolved. **e**, The S3H3 binding on SD1 of protomer 2. **f**, The structural elements involved in the interaction between S3H3 Fab and SD1 are labelled. The SD1 T547K substitution is also shown in red. The residues of SD1 in proximity to S3H3 (less than 4 Å) are indicated and coloured in transparent orange (related to Extended Data Table 4). **g**, The SD1–S3H3 interaction interface analysed using PISA, with the major involved structural elements labelled (the spring represents the salt bridge, and the black dashed line represents the hydrogen bond).

Omicron S in complex with S3H3 Fab. Both structures showed two engaged Fab densities on the SD1 of protomer 2 and protomer 3, but with the RBD-1 in the up (termed Omicron S-open–S3H3) or down (termed Omicron S-close–S3H3) conformations (Fig. 4a, b). The two maps were resolved to the resolution of 3.48 Å and 3.64 Å, respectively (Extended Data Fig. 5, Extended Data Table 1). Compared with the Omicron S-open, the S trimer in S-open–S3H3 exhibits a slight twist and the RBD-1 displays a 9.1° downward rotation (Fig. 4c), making the S trimer seemingly less 'open' as a whole. SD1 shows a slight downward rotation (Fig. 4c).

We further focus-refined the SD1–S3H3 Fab region and obtained a map at 3.61 Å resolution, with most of the side chain densities well resolved (Fig. 4d). The heavy chain of S3H3 Fab contributes more to the interactions with SD1 than the light chain does, that is, all three heavy-chain complementarity determining regions (CDRs) of S3H3 and its CDRL1 and CDRL3 interact with T323–E324 and the three loops (loop$^{532–537}$, loop$^{554–556}$ and loop$^{581–584}$) of SD1 (Fig. 4e, f, Extended Data Table 4). Specifically, S32 of CDRL1 forms hydrogen bonds with S555 and I584 of SD1, respectively, D102 of CDRH3 forms a hydrogen bond with T581 from loop$^{581–584}$, and D55 of CDRH2 forms a salt bridge with K537 from loop$^{532–537}$ (Fig. 4g, Extended Data Table 4), thus constituting an intense interaction network between S3H3 Fab and SD1. A single mutation, T547K, is present in the SD1 of Omicron; however, this mutation was located outside the footprint of S3H3 (Fig. 4f), and thus will not affect the Omicron S–S3H3 interaction. Collectively, S3H3 binds to the extremely conserved SD1 region, therefore retains binding and neutralizing activity towards major VOCs including Omicron.

Discussion

In this study, we performed cryo-EM and biochemical analysis on the Omicron S trimer and its complex with the ACE2 receptor. We captured both the closed and the open states of the Omicron S trimer (Fig. 1a). In contrast to the S trimer of the Delta, Beta and Kappa variants[10,31], the

Omicron S-close and S-open structures appear more twisted and compact than their counterpart of the G614 strain[1] (Fig. 1d, e), which may hinder its spike transformation towards the fusion-prone open state and shielding of S1. This could be related to enhanced inter-protomer and S1–S2 interactions induced by unique Omicron substitutions (T547K, N856K and N764K in SD1 and S2) (Fig. 1g).

Corroborating to the enhanced inter-protomer and S1–S2 interactions of Omicron, our cryo-EM analysis revealed that for the Omicron S trimer, the dominantly populated conformation is the closed state with all the RBDs buried, possibly leading to 'conformational masking' that may prevent antibody binding and neutralization at sites of receptor binding, similar to that described for the HIV-1 envelope[47,48]. Such an Omicron conformational masking mechanism could potentially affect antibodies that bind to the up RBDs (such as classes 1, 2 and 4 RBD antibodies[49]), contributing to the observed extensive neutralization escape by Omicron. However, for the Delta S trimer, our recent work showed that the dominant population is in the open state, indicating that the conformational masking mechanism may be less effective for the Delta variant[31,35]. This could contribute to the striking immune evasion of the Omicron variant[15,17–22].

We also captured three states for the Omicron S–ACE2 complex (Fig. 2b). Unlike the Delta S, which tends to bind to three ACE2 in majority[31], Omicron mainly binds to one or two ACE2 (Extended Data Fig. 3b). Further focus-refining of the RBD-1–ACE2 structure demonstrated that the substitutions on the RBM of Omicron (especially Q493R, G496S, Q498R, S477N and Y505H) result in the formation of new salt bridges and hydrogen bonds, and more complementary electrostatic surface properties (Fig. 2d, f, g), which together may compensate the abolished original RBM–ACE2 interactions[26,43,44], leading to enhanced interactions with ACE2 and potentially enhanced transmissibility of the Omicron variant.

The present study showed that 2H2 and S3H3 retain potent neutralization towards Omicron and Delta (Fig. 3). Further structural study revealed a unique binding epitope of S3H3 within the SD1 region (Fig. 4). The binding of S3H3 to S trimer may function as a 'lock' to block the releasing of S1 from S2, resulting in inhibition of virus entry. The SD1 region targeted by S3H3 is extremely conserved among SARS-CoV-2 variants (Fig. 4f), thus explaining the cross-neutralization ability of S3H3 towards Omicron, Delta and other variants[46]. These findings also suggest a possibility to design SD1-based broad-spectrum SARS-CoV-2 vaccines. It is somewhat surprising that 2H2, whose epitope largely overlaps with RBM[45], remained highly neutralizing against Omicron, despite the loss of the neutralization potency of this antibody to the Kappa and Beta variants due to their E484Q or E484K substitution[10]. Docking of our previous RBD-bound 2H2 Fab structure[45] onto our current Omicron RBD-1 structure from the S-open state revealed that the 2H2 Fab could be reasonably well accommodated without major clashes with RBD (Extended Data Fig. 6a). In particular, the E484A substitution in Omicron does not appear to create steric hindrance with 2H2 due to the smaller size of the Ala side chain. In addition, the Omicron RBM substitutions, such as Q493R, Q498R and Y505H, do not introduce extra clashes between RBM and 2H2, and also make the epitope surface more positively charged than the WT RBD-1 (ref. [45]) (Extended Data Fig. 6b), potentially allowing better interaction with the 2H2 paratope, which tends to be more negatively charged (Extended Data Fig. 6c).

We found that Omicron could escape three RBD antibodies, including 8D3, S5D2 and 3C1 (refs. [45,46]). Both 8D3 and S5D2 are class 1 RBD antibodies and they share similar epitopes centred around loop[477–489] (refs. [31,46]). Docking of the RBD-bound 8D3 or S5D2 Fab structures[31,46] onto the Omicron RBD-1 structure revealed that several Omicron residues, especially S477N, may potentially clash with the 8D3 Fab (Extended Data Fig. 6d); the S477N and T478K substitutions in Omicron may break the hydrogen bond network between RBD and S5D2 Fabs (Extended Data Fig. 6e). 3C1, whose epitope mainly involves the relatively stable RBD core[45], belongs to the class 3 RBD antibody[49]. Analysis of the docked 3C1 structure on the Omicron RBD-1 showed that the S375F substitution may contribute to the escape of Omicron from 3C1 binding and neutralization through altering the interaction interface (Extended Data Fig. 6f).

In summary, the present study reveals that the Omicron spike acquires an increased RBM–ACE2 interaction network contributed by new hydrogen bonds and salt bridges and more favourable surface properties, and therefore maintains a strong affinity to ACE2, providing a possible explanation to the high infectivity and transmissibility of Omicron. In addition, our study suggests that, besides individual residue substitutions in RBD antibody epitopes, a conformational masking mechanism may also contribute to the extensive antibody evasion by Omicron. Moreover, our work demonstrates that Omicron remains sensitive to S3H3, an antibody that targets the extremely conserved SD1 region. Our findings provide structural insights into how Omicron maintains high transmissibility while greatly evading immunity, and may also inform design of broadly effective vaccines against emerging variants.

Online content

Any methods, additional references, Nature Research reporting summaries, source data, extended data, supplementary information, acknowledgements, peer review information; details of author contributions and competing interests; and statements of data and code availability are available at https://doi.org/10.1038/s41586-022-04581-9.

1. Zhang, J. et al. Structural impact on SARS-CoV-2 spike protein by D614G substitution. *Science* **372**, 525–530 (2021).
2. Grabowski, F., Preibisch, G., Gizinski, S., Kochanczyk, M. & Lipniacki, T. SARS-CoV-2 variant of concern 202012/01 has about twofold replicative advantage and acquires concerning mutations. *Viruses* **13**, 392 (2021).
3. Wise, J. Covid-19: new coronavirus variant is identified in UK. *Brit. Med. J.* **371**, m4857 (2020).
4. Davies, N. G. et al. Estimated transmissibility and impact of SARS-CoV-2 lineage B.1.1.7 in England. *Science* **372**, eabg3055 (2021).
5. Gobeil, S. M. et al. Effect of natural mutations of SARS-CoV-2 on spike structure, conformation, and antigenicity. *Science* **373**, eabi6226 (2021).
6. Cai, Y. et al. Structural basis for enhanced infectivity and immune evasion of SARS-CoV-2 variants. *Science* **373**, 642–648 (2021).
7. Yuan, M. et al. Structural and functional ramifications of antigenic drift in recent SARS-CoV-2 variants. *Science* **373**, 818–823 (2021).
8. Tegally, H. et al. Detection of a SARS-CoV-2 variant of concern in South Africa. *Nature* **592**, 438–443 (2021).
9. Msomi, N., Mlisana, K. & de Oliveira, T., Network for Genomic Surveillance in South Africa writing group. A genomics network established to respond rapidly to public health threats in South Africa. *Lancet Microbe* **1**, e229–e230 (2020).
10. Wang, Y. et al. Conformational dynamics of the Beta and Kappa SARS-CoV-2 spike proteins and their complexes with ACE2 receptor revealed by cryo-EM. *Nat. Commun.* **12**, 7345 (2021).
11. Voloch, C. M. et al. Genomic characterization of a novel SARS-CoV-2 lineage from Rio de Janeiro, Brazil. *J. Virol.* **95**, e00119–21 (2021).
12. Singh, J., Rahman, S. A., Ehtesham, N. Z., Hira, S. & Hasnain, S. E. SARS-CoV-2 variants of concern are emerging in India. *Nat. Med.* **27**, 1131–1133 (2021).
13. Winger, A. & Caspari, T. The spike of concern—the novel variants of SARS-CoV-2. *Viruses* **13**, 1002 (2021).
14. WHO. Enhancing readiness for Omicron (B.1.1.529): technical brief and priority actions for Member States. *WHO* https://www.who.int/publications/m/item/enhancing-readiness-for-omicron-(b.1.1.529)-technical-brief-and-priority-actions-for-member-states (2021).
15. Cameroni, E. et al. Broadly neutralizing antibodies overcome SARS-CoV-2 Omicron antigenic shift. *Nature* **602**, 664–670 (2021).
16. Mannar, D. et al. SARS-CoV-2 Omicron variant: antibody evasion and cryo-EM structure of spike protein-ACE2 complex. *Science* **375**, 760–764 (2022).
17. Hoffmann, M. et al. The Omicron variant is highly resistant against antibody-mediated neutralization—implications for control of the COVID-19 pandemic. *Cell* **185**, 447–456.e11 (2021).
18. Carreño, J. M. et al. Activity of convalescent and vaccine serum against SARS-CoV-2 Omicron. *Nature* **602**, 682–688 (2021).
19. Liu, L. et al. Striking antibody evasion manifested by the Omicron variant of SARS-CoV-2. *Nature* **602**, 676–681 (2021).
20. Cao, Y. et al. Omicron escapes the majority of existing SARS-CoV-2 neutralizing antibodies. *Nature* **602**, 657–663 (2022).
21. Planas, D. et al. Considerable escape of SARS-CoV-2 Omicron to antibody neutralization. *Nature* **602**, 671–675 (2022).
22. Cele, S. et al. Omicron extensively but incompletely escapes Pfizer BNT162b2 neutralization. *Nature* **602**, 654–656 (2022).

23. Tang, T., Bidon, M., Jaimes, J. A., Whittaker, G. R. & Daniel, S. Coronavirus membrane fusion mechanism offers a potential target for antiviral development. *Antiviral Res.* **178**, 104792 (2020).
24. Rabaan, A. A. et al. SARS-CoV-2, SARS-CoV, and MERS-CoV: a comparative overview. *Infez. Med.* **28**, 174–184 (2020).
25. Wang, Q. et al. Structural and functional basis of SARS-CoV-2 entry by using human ACE2. *Cell* **181**, 894–904.e9 (2020).
26. Lan, J. et al. Structure of the SARS-CoV-2 spike receptor-binding domain bound to the ACE2 receptor. *Nature* **581**, 215–220 (2020).
27. Shang, J. et al. Structural basis of receptor recognition by SARS-CoV-2. *Nature* **581**, 221–224 (2020).
28. Yin, W. et al. Structures of the Omicron spike trimer with ACE2 and an anti-Omicron antibody. *Science* **375**, 1048–1053 (2022).
29. Toelzer, C. et al. Free fatty acid binding pocket in the locked structure of SARS-CoV-2 spike protein. *Science* **370**, 725–730 (2020).
30. Punjani, A., Rubinstein, J. L., Fleet, D. J. & Brubaker, M. A. cryoSPARC: algorithms for rapid unsupervised cryo-EM structure determination. *Nat. Methods* **14**, 290–296 (2017).
31. Wang, Y. et al. Structural basis for SARS-CoV-2 Delta variant recognition of ACE2 receptor and broadly neutralizing antibodies. *Nat. Commun.* **13**, 871 (2022).
32. Cai, Y. et al. Distinct conformational states of SARS-CoV-2 spike protein. *Science* **369**, 1586–1592 (2020).
33. Walls, A. C. et al. Structure, function, and antigenicity of the SARS-CoV-2 spike glycoprotein. *Cell* **181**, 281–292.e6 (2020).
34. Wrapp, D. et al. Cryo-EM structure of the 2019-nCoV spike in the prefusion conformation. *Science* **367**, 1260–1263 (2020).
35. Xu, C. et al. Conformational dynamics of SARS-CoV-2 trimeric spike glycoprotein in complex with receptor ACE2 revealed by cryo-EM. *Sci. Adv.* **7**, eabe5575 (2021).
36. Henderson, R. et al. Controlling the SARS-CoV-2 spike glycoprotein conformation. *Nat. Struct. Mol. Biol.* **27**, 925–933 (2020).
37. Benton, D. J. et al. Receptor binding and priming of the spike protein of SARS-CoV-2 for membrane fusion. *Nature* **588**, 327–330 (2020).
38. Berger, I. & Schaffitzel, C. The SARS-CoV-2 spike protein: balancing stability and infectivity. *Cell Res.* **30**, 1059–1060 (2020).
39. Cui, Z. et al. Structural and functional characterizations of infectivity and immune evasion of SARS-CoV-2 Omicron. *Cell* **185**, 860–871.e13 (2022).
40. Han, P. et al. Receptor binding and complex structures of human ACE2 to spike RBD from Omicron and Delta SARS-CoV-2. *Cell* **185**, 630–640 (2022).
41. Lan, J. *et al*. Structural and computational insights into the SARS-CoV-2 Omicron RBD-ACE2 interaction. Preprint at *bioRxiv* https://doi.org/10.1101/2022.01.03.474855 (2022).
42. McCallum, M. et al. Structural basis of SARS-CoV-2 Omicron immune evasion and receptor engagement. *Science* **375**, 864–868 (2022).
43. Mannar, D. et al. Structural analysis of receptor binding domain mutations in SARS-CoV-2 variants of concern that modulate ACE2 and antibody binding. *Cell Rep.* **37**, 110156 (2021).
44. Laffeber, C., de Koning, K., Kanaar, R. & Lebbink, J. H. G. Experimental evidence for enhanced receptor binding by rapidly spreading SARS-CoV-2 variants. *J. Mol. Biol.* **433**, 167058 (2021).
45. Zhang, C. et al. Development and structural basis of a two-mAb cocktail for treating SARS-CoV-2 infections. *Nat. Commun.* **12**, 264 (2021).
46. Xu, S. et al. Mapping cross-variant neutralizing sites on the SARS-CoV-2 spike protein. *Emerg. Microbes Infect.* **11**, 351–367 (2021).
47. Kwong, P. D. et al. HIV-1 evades antibody-mediated neutralization through conformational masking of receptor-binding sites. *Nature* **420**, 678–682 (2002).
48. Munro, J. B. et al. Conformational dynamics of single HIV-1 envelope trimers on the surface of native virions. *Science* **346**, 759–763 (2014).
49. Barnes, C. O. et al. SARS-CoV-2 neutralizing antibody structures inform therapeutic strategies. *Nature* **588**, 682–687 (2020).

Methods

Protein expression and purification

To express the SARS-CoV-2 Omicron variant S glycoprotein ectodomain, the mammalian codon-optimized gene-coding SARS-CoV-2 (hCoV-19 Botswana R42B90_BHP_000842207 2021, GISAID ID: EPI_ISL_6752027) S glycoprotein ectodomain with double proline substitutions and 'GSAS' substitution at the furin cleavage site was cloned into the pcDNA 3.1+ vector[35]. A C-terminal T4 fibritin trimerization motif, a TEV protease cleavage site, a FLAG tag and a His tag were cloned downstream of the S glycoprotein ectodomain (Extended Data Fig. 1a). The constructs of prefusion-stabilized S proteins of SARS-CoV-2 G614 and Delta (B.1.617.2) variants were prepared as previously reported[31]. A gene encoding the human ACE2 peptidase domain (Q18–D615) with an N-terminal IL-10 signal peptide and a C-terminal His tag was cloned into the pcDNA 3.4 vector[35]. The recombinant proteins were prepared as previously reported in a published protocol[35]. In brief, the constructs were transiently transfected into HEK293F cells (Thermo Fisher) using polyethylenimine (PEI). Note that the HEK293F cell line has not recently been tested for mycoplasma contamination. Three days after transfection, the supernatants were harvested by centrifugation, and then passed through 0.45-μm filter membrane. The clarified supernatants were added with 20 mM Tris-HCl pH 7.5, 200 mM NaCl, 20 mM imidazole and 4 mM $MgCl_2$, and incubated with Ni-NTA resin at 4 °C for 1 h. The Ni-NTA resin was recovered and washed with 20 mM Tris-HCl pH 7.5, 200 mM NaCl and 20 mM imidazole. The protein was eluted by 20 mM Tris-HCl pH 7.5, 200 mM NaCl and 250 mM imidazole.

Biolayer interferometry assay

Before the biolayer interferometry (BLI) assay, Ni-NTA-purified recombinant S trimer proteins of the G614, Delta and Omicron SARS-CoV-2 variants were further purified by gel-filtration chromatography using a Superose 6 increase 10/300 GL column (GE Healthcare) pre-equilibrated with PBS. Then, 70 μg of purified S trimer proteins of the G614, Delta and Omicron variants were separately biotinylated using the EZ-Link Sulfo-NHS-LC-LC-Biotin kit (Thermo Fisher) and then purified by Zeba spin desalting columns (Thermo Fisher).

Binding affinities of S trimers to ACE2 were determined by BLI analysis on an Octet Red96 instrument (Pall FortéBio). In brief, biotinylated S trimer proteins (approximately 40 μg ml^{-1}) were immobilized onto streptavidin (SA) biosensors (Pall FortéBio). After washing with kinetic buffer (0.01 M PBS with 0.02% Tween 20 and 0.1% bovine serum albumin), these sensors were incubated with threefold serial dilutions of ACE2 monomer protein for 500 s. Subsequently, the biosensors were allowed to dissociate in kinetic buffer for 500 s. The data were analysed using the Octet Data Analysis 11.0 software to calculate affinity constants.

Neutralization

Luciferase (Luc)-expressing pseudoviruses bearing SARS-CoV-2 S proteins were constructed based on the HIV-1 backbone. In brief, HEK 293T cells (American Type Culture Collection) in a 10-cm dish were co-transfected using PEI (polysciences) with 10 μg pCMV-dR8.91 packaging plasmid, 10 μg recombinant pLVX-IRES-ZsGreen1 plasmid containing the luciferase reporter gene, and 2 μg recombinant pVAX1 plasmids encoding the SARS-CoV-2 S proteins. The cells were incubated with the transfection mixture for 6 h, and then 5 ml of fresh DMEM medium with 10% FBS was added to each dish. After incubation overnight, the media in the dishes were replaced with fresh DMEM medium (10% FBS). At 48 h post-transfection, the culture supernatant was harvested and frozen at −80 °C before use.

All mAbs were fourfold serially diluted and tested by a pseudovirus neutralization assay with human ACE2-overexpressing HEK 293T cells (293T-hACE2), which were generated in our previous study and verified by western blot, following our previous protocol[45]. Note that the 293T-hACE2 cell line has not recently been tested for mycoplasma contamination. Two days after pseudovirus infection, luciferase activity was measured. Data were analysed by non-linear regression using GraphPad Prism 8 to calculate the IC_{50}.

ELISA

To test the binding activities of recombinant Omicron S protein with our previously developed anti-SARS-CoV-2 mAbs[45,46], recombinant S trimer proteins from WT[45], Delta or Omicron SARS-CoV-2 strains were twofold serially diluted and coated onto ELISA plates at 37 °C for 2 h. The plates were blocked with 5% milk in PBS-Tween 20 (PBST) at 37 °C for 1 h. After washing with PBST, the plates were incubated with 50 ng per well of each of the anti-SARS-CoV-2 mAbs[45,46] at 37 °C for 2 h, followed by horseradish peroxidase (HRP)-conjugated anti-mouse IgG (1:5,000 dilution; Sigma) at 37 °C for 1 h. After washing and colour development, absorbance was measured at 450 nm. ELISA data were analysed by non-linear regression using GraphPad Prism 8. Note that for neutralization and ELISA assays, no statistical method was used to predetermine sample size, and no blinding or randomization protocols were used.

Omicron S–S3H3 Fab complex formation

The Omicron S–S3H3 Fab complex was prepared following our previously reported protocol[46]. In brief, purified S3H3 IgG was incubated with papain (300:1 w/w) in PBS buffer (in the presence of 20 mM L-cysteine and 1 mM EDTA) for 3 h at 37 °C. The reaction was quenched by 20 mM iodoacetamide. Fab was purified by running over a HiTrap DEAE FF column (GE Healthcare) pre-equilibrated with PBS. Omicron S protein was incubated with S3H3 Fab in a 1:6 molar ratio on ice for 1 h. The Omicron S–S3H3 Fab complex was purified by size-exclusion chromatography using a Superose 6 increase 10/300 GL column (GE Healthcare) in 20 mM Tris-HCl pH 7.5, 200 mM NaCl and 4% glycerol. The complex peak fractions were concentrated and assessed by SDS–PAGE.

Cryo-EM

Sample preparation. To prepare the cryo-EM sample of the Omicron S trimer, a 2.2 μl aliquot of the sample was applied on a plasma-cleaned holey carbon grid (R 1.2/1.3, Cu, 200 mesh; Quantifoil). The grid was blotted with Vitrobot Mark IV (Thermo Fisher Scientific) at 100% humidity and 8 °C, and then plunged into liquid ethane cooled by liquid nitrogen. To prepare the cryo-EM sample of the Omicron S–ACE2 complex, the purified Omicron S trimer was incubated with ACE2 in a 1:4 molar ratio on ice for 20 min and then vitrified using the same condition. The purified Omicron S–S3H3 complex was vitrified using the same procedure as for the Omicron S sample.

Data collection. Cryo-EM movies of the samples were collected on a Titan Krios electron microscope (Thermo Fisher Scientific) operated at an accelerating voltage of 300 kV. For the three datasets, the movies were collected at a magnification of ×64,000 and recorded on a K3 direct electron detector (Gatan) operated in the counting mode (yielding a pixel size of 1.093 Å), and under a low-dose condition in an automatic manner using EPU 2.11 software (Thermo Fisher Scientific). Each frame was exposed for 0.1 s, and the total exposure time was 3 s, leading to a total accumulated dose of 50.2 $e^-/Å^2$ on the specimen.

3D reconstruction. For each dataset, the motion correction of image stack was performed using the embedded module Motioncor2 in Relion 3.1 (refs. [35,50,51]), and CTF parameters were determined using CTFFIND4.1.8 (ref. [52]) before further data processing. Unless otherwise described, the data processing was performed in Relion 3.1.

For the Omicron S dataset (Extended Data Fig. 2), 600,845 particles remained after reference-free 2D classification in cryoSPARC v3.3.1 (ref. [30]).

After two rounds of 3D classification and further focused 3D classification on the RBD-1 region, we obtained an Omicron S-close map from 108,509 particles and an RBD-1-up open conformation from 69,873 particles. We then preformed focused 3D classification on the RBD-3 region of the open-state dataset and obtained an Omicron S-open map from 30,967 particles and a S-open-2 map from 38,906 particles. After Bayesian polishing and CTF refinement, the Omicron S-close, S-open and S-open-2 datasets were independently loaded into cryoSPARC v3.3.1 (ref. [30]) and refined to the resolution of 3.08 Å, 3.40 Å and 3.41 Å, respectively, using non-uniform refinement. The overall resolutions for all of the cryo-EM maps in this study were determined based on the gold-standard criterion using a Fourier shell correlation (FSC) of 0.143. Moreover, we performed 3D variability analysis on the Omicron S trimer dataset containing 178,382 particles in cryoSPARC v3.3.1 to capture its continuous conformational dynamics[30].

For the Omicron S–ACE2 dataset (Extended Data Fig. 3), 1,268,072 particles remained after reference-free 2D classification. After two rounds of 3D classification and further focused 3D classification on the RBD-1–ACE2 region, we obtained an Omicron S–ACE2 map from 141,538 particles. After Bayesian polishing and CTF refinement, the map was reconstructed to 3.53 Å resolution. We then focused on the RBD-2 region for further classification and obtained two conformations, with RBD-2 in the 'down' position (43.9%), termed S–ACE2-C1, or in the 'up' position. The RBD-2 up dataset was further focused 3D classified on the RBD-3 region. We then obtained two conformations with RBD-3 in the down or up position, termed S–ACE2-C2 and S–ACE2-C3, respectively. The three datasets were independently loaded into cryoSPARC v3.3.1 and refined using non-uniform refinement to 3.69 Å, 3.70 Å and 4.04 Å resolution, respectively. Here, after obtaining the 3.53 Å resolution map of Omicron S–ACE2, we performed further local refinement on the RBD-1–ACE2 region (indicated by a black dotted ellipsoid in Extended Data Fig. 3a) in cryoSPARC v3.3.1 to acquire a 3.67 Å resolution map of this region.

For the Omicron S–S3H3 dataset (Extended Data Fig. 5), a similar data processing procedure was adapted as described for the Omicron S dataset to obtain a 3.56 Å resolution S–S3H3 map from 238,121 particles. We then carried out focused 3D classification on the RBD-1 region, followed by non-uniform refinement in cryoSPARC v3.3.1, and obtained a 3.48 Å resolution S-open–S3H3 map from 162,221 particles and a 3.64 Å resolution S-close–S3H3 map from 75,900 particles. In addition, after obtaining the 3.56 Å resolution map, we performed focused 3D classification on the S3H3–SD1 region of protomer 2 (highlighted by an orange dotted ellipsoid in Extended Data Fig. 5), leading to a dataset of 101,192 particles, which was further local refined on the S3H3–SD1 region in cryoSPARC v3.3.1, deducing a 3.61 Å resolution map of this region. All of the obtained maps were post-processed through deepEMhancer[53].

Atomic model building

To build an atomic model for the Omicron S-open structure, we used the atomic model of Delta S-open (PDB: 7W92) from our previous study as the initial model[31]. We first fit the model into our Omicron S-open map in Chimera by rigid body fitting, then manually substituted the mutations of the Omicron variant in COOT[54]. Subsequently, we flexibly refined the model against our Omicron S-open map using ROSETTA[55]. Finally, we used the phenix.real_space_refine module in Phenix 1.19.2-4158 for the S trimer model refinement against the map[56]. For the S-close model, we utilized the down protomer from our recent Delta S-transition (PDB: 7W94)[31] structure as the initial template, and followed a similar procedure described above for model refinement. For the Omicron S–ACE2 and the local refined RBD-1–ACE2 structures, we used the Delta S–ACE2 model (PDB: 7W98 and 7W9I)[31] as the initial template, and followed a similar procedure described above for model refinement. For better fitting in the dynamic ACE2 region of the Omicron S–ACE2-C1, C2, and C3 maps, we merged the better resolved Omicron RBD-1–ACE2 model with the other portion of the original model to make a complete model, and refined it against the corresponding unsharpened map. For the Omicron S–S3H3 and the local refined RBD-1–S3H3 structures, we utilized our recent Beta S–S3H3 model (PDB: 7WDF and 7WD8)[46] as the template, and followed a similar procedure described above for model refinement. The atomic models were validated using the Phenix.molprobity command in Phenix. Analyses of the interaction interface were conducted through the PISA server[57].

UCSF Chimera and ChimeraX were applied for figure generation, rotation measurement and Coulombic potential surface analysis[58,59].

Reporting summary

Further information on research design is available in the Nature Research Reporting Summary linked to this paper.

Data availability

The cryo-EM maps determined for the Omicron S trimer have been deposited at the Electron Microscopy Data Bank with the accession codes EMD-32556, EMD-32854 and EMD-32855, and the associated atomic models have been deposited in the PDB with the accession codes 7WK2, 7WVN and 7WVO for S-close, S-open and S-open-2 states, respectively. For the S–ACE2 dataset, related cryo-EM maps have been deposited in the Electron Microscopy Data Bank with the accession codes EMD-32558, EMD-32856, EMD-32857 and EMD-32560, and the associated models have been deposited in the PDB with the accession codes 7WK4, 7WVP, 7WVQ and 7WK6 for S–ACE2-C1, S–ACE2-C2, S–ACE-C3 and RBD-1–ACE2, respectively. For the S–S3H3 Fab dataset, related cryo-EM maps have been deposited in the Electron Microscopy Data Bank with the accession codes EMD-32562, EMD-32563 and EMD-32564, and the associated models have been deposited in the PDB with the accession codes 7WK8, 7WK9 and 7WKA for SD1–S3H3, S-open–S3H3 and S-close–S3H3, respectively. The structures used for the initial templates or structural analysis in this work include PDB IDs: 7W92, 7W94, 7W98, 7W9I, 7WDF, 7WD8, 7KRQ, 7KRR, 6M0J, 7DK4, 7WCR, 7W9F and 7DCC. For gel source images, see Supplementary Fig. 1. Source data are provided with this paper.

50. Zheng, S. Q. et al. MotionCor2: anisotropic correction of beam-induced motion for improved cryo-electron microscopy. *Nat. Methods* **14**, 331–332 (2017).
51. Fernandez-Leiro, R. & Scheres, S. H. W. A pipeline approach to single-particle processing in RELION. *Acta Crystallogr. D Struct. Biol.* **73**, 496–502 (2017).
52. Rohou, A. & Grigorieff, N. CTFFIND4: fast and accurate defocus estimation from electron micrographs. *J. Struct. Biol.* **192**, 216–221 (2015).
53. Sanchez-Garcia, R. et al. DeepEMhancer: a deep learning solution for cryo-EM volume post-processing. *Commun. Biol.* **4**, 874 (2021).
54. Emsley, P. & Cowtan, K. Coot: model-building tools for molecular graphics. *Acta Crystallogr. D Biol. Crystallogr.* **60**, 2126–2132 (2004).
55. DiMaio, F. et al. Atomic-accuracy models from 4.5-Å cryo-electron microscopy data with density-guided iterative local refinement. *Nat. Methods* **12**, 361–365 (2015).
56. Adams, P. D. et al. PHENIX: a comprehensive Python-based system for macromolecular structure solution. *Acta Crystallogr. D Biol. Crystallogr.* **66**, 213–221 (2010).
57. Krissinel, E. & Henrick, K. Inference of macromolecular assemblies from crystalline state. *J. Mol. Biol.* **372**, 774–797 (2007).
58. Pettersen, E. F. et al. UCSF Chimera—a visualization system for exploratory research and analysis. *J. Comput. Chem.* **25**, 1605–1612 (2004).
59. Goddard, T. D. et al. UCSF ChimeraX: meeting modern challenges in visualization and analysis. *Protein Sci.* **27**, 14–25 (2018).

Acknowledgements We are grateful to the staff at the NCPSS Electron Microscopy facility, Database and Computing facility, and Protein Expression and Purification facility for instrument support and technical assistance. This work was supported by grants from the Strategic Priority Research Program of CAS (XDB37040103 and XDB29040300), National Key R&D Program of China (2017YFA0503503 and 2020YFC0845900), the NSFC (32130056 and 31872714), Shanghai Academic Research Leader (20XD1404200), Shanghai Pilot Program for Basic Research–CAS, Shanghai Branch (JCYJ--SHFY-2022-008) and the European Union's Horizon 2020 research and innovation programme under grant agreement (no. 101003589). C.Z. is supported by the Youth Innovation Promotion Association of CAS and Shanghai Rising-Star Program (21QA1410000). C.X. is supported by the China National Postdoctoral Program for Innovative Talents (BX2021310), Shanghai Super Postdoctoral Incentive Plan.

Author contributions Y.C. and Z.H. designed the experiments. Yanxing Wang expressed and purified the proteins with the assistance of Z.L. and S.X. Q.H. and W.H. performed cryo-EM

data acquisitions. Q.H., W.H., J.L. and Yifan Wang performed cryo-EM reconstructions and model buildings. C.Z. and S.X. performed biochemical analyses. J.L., Q.H., W.H., Yifan Wang, C.X. and C.Z. analysed the data. Y.C., Z.H., Q.H., J.L., W.H., Yanxing Wang and C.Z. wrote the manuscript.

Competing interests Institut Pasteur of Shanghai is in the process of applying for a patent application (no. 202110713023.7) covering anti-SARS-CoV-2 mAb S3H3 that lists Z.H., S.X. and C.Z. as inventors. The other authors declare no competing interests.

Additional information

Supplementary information The online version contains supplementary material available at https://doi.org/10.1038/s41586-022-04581-9.

Correspondence and requests for materials should be addressed to Yanxing Wang, C. Z., Z. H. or Y. C.

Peer review information *Nature* thanks Nadav Elad and the other, anonymous, reviewer(s) for their contribution to the peer review of this work. Peer reviewer reports are available.

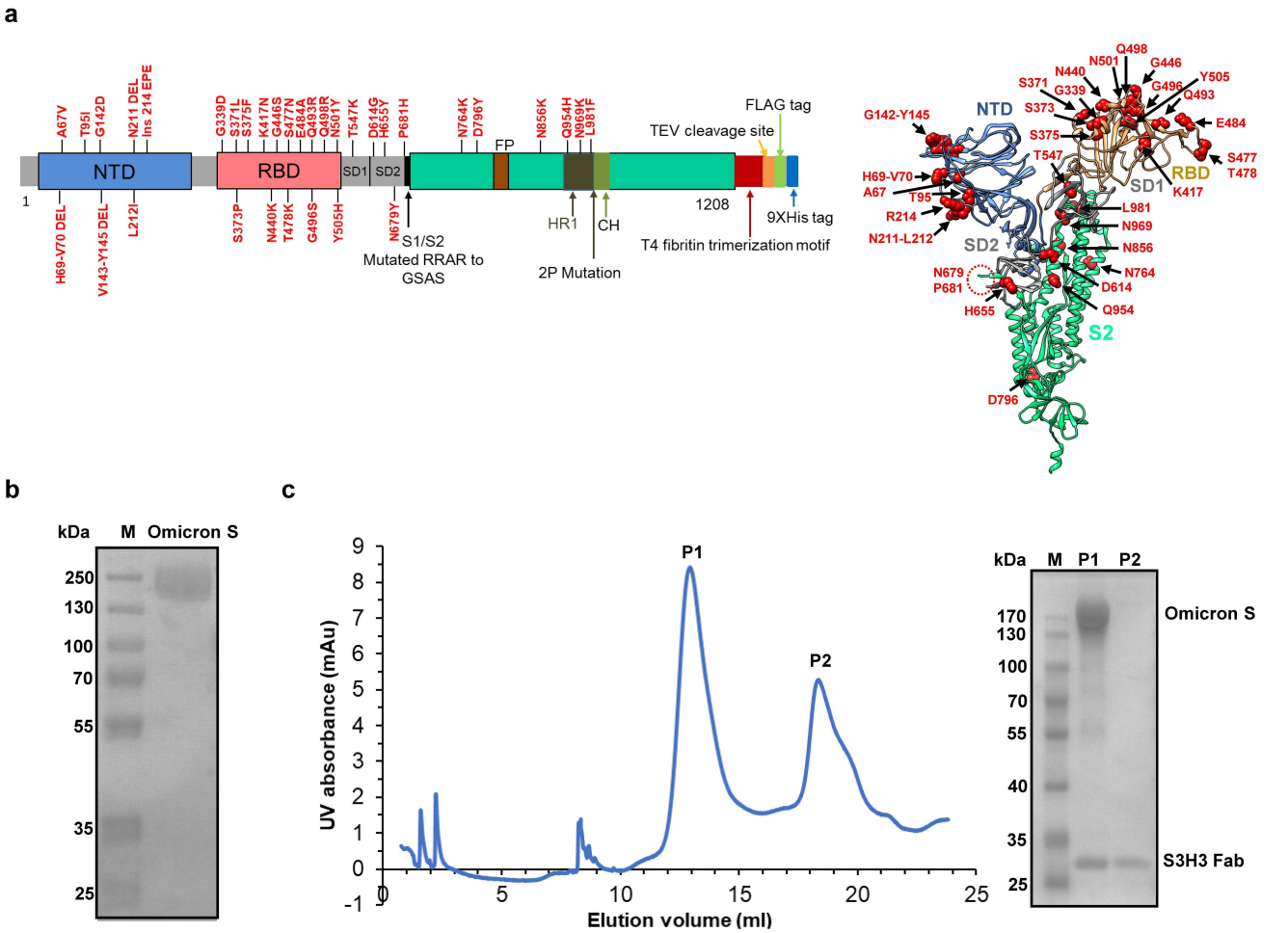

Extended Data Fig. 1 | Purification of Omicron variant S and S-S3H3 Fab complex. a, Schematic diagram of the Omicron variant S organization in this study (left, positions of all mutations are indicated), and the model of a SARS-CoV-2 S protomer (right) with mutation sites of the Omicron variant shown as red sphere. **b**, SDS-PAGE analysis of the purified Omicron variant S protein. Representative images of two independent experiments are shown. For gel source data, related to Supplementary Fig. 1. **c**, Size-exclusion chromatogram and SDS-PAGE analysis of the formed Omicron S-S3H3 Fab complex. Representative images of two independent experiments are shown. For gel source data, related to Supplementary Fig. 1.

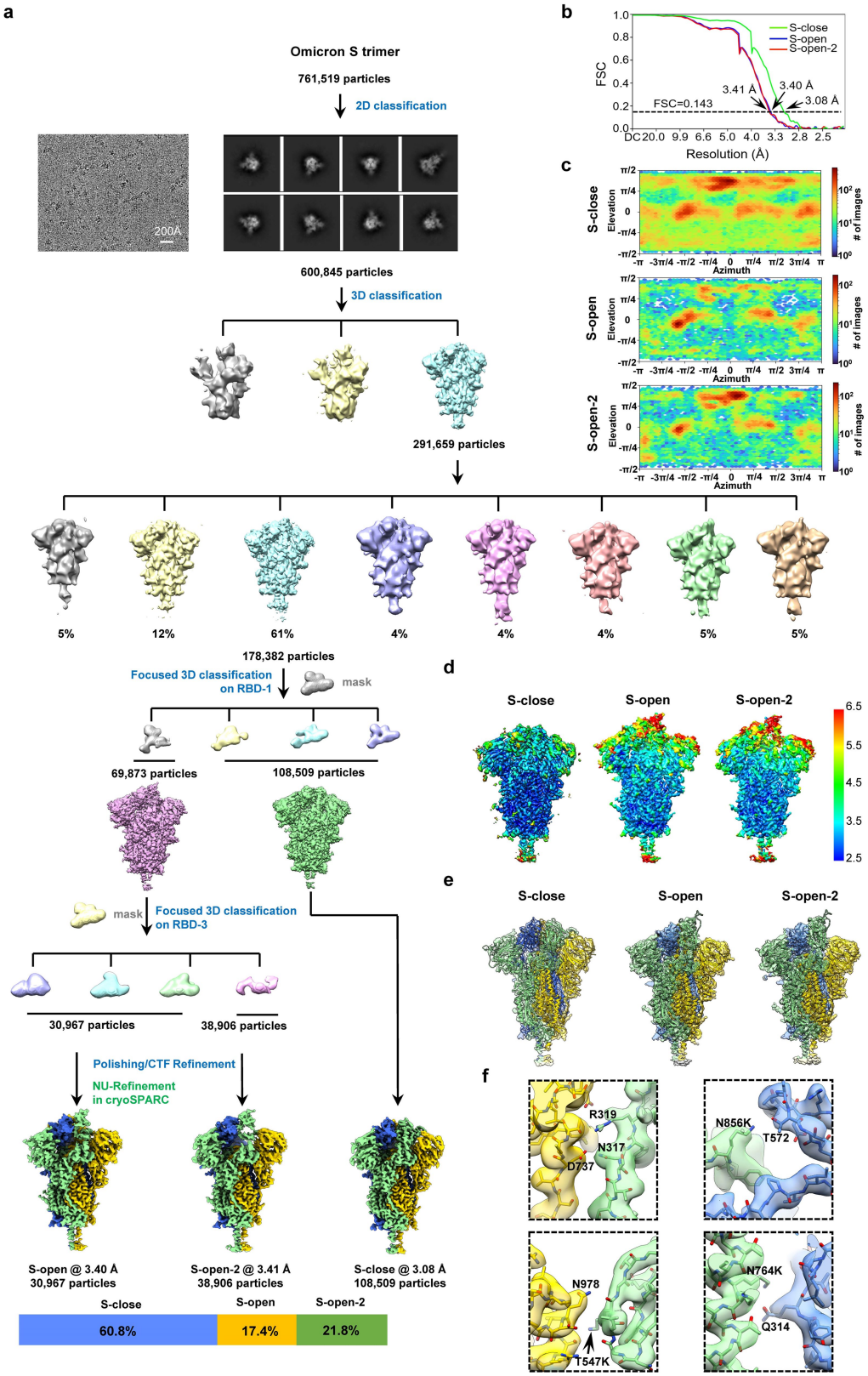

Extended Data Fig. 2 | Cryo-EM analysis on the Omicron S trimer. a, Data processing workflow for structure determination of the Omicron S trimer. A representative original micrograph, reference-free 2D class averages, and the population distributions of the Omicron S-close, S-open, and S-open-2 states are also presented. **b**, Resolution assessment of the Omicron S-close, S-open, and S-open-2 maps by FSC at 0.143 criterion. **c**, **d**, Angular distribution (**c**) and local resolution evaluation (**d**) of the S-close, S-open, and S-open-2 maps. **e**, Model-map fitting for each of the three structures. **f**, Model and map fitting in the inter-protomer interaction area of Omicron S-close. Protomer 1, 2, and 3 are colored in light green, royal blue and gold, respectively.

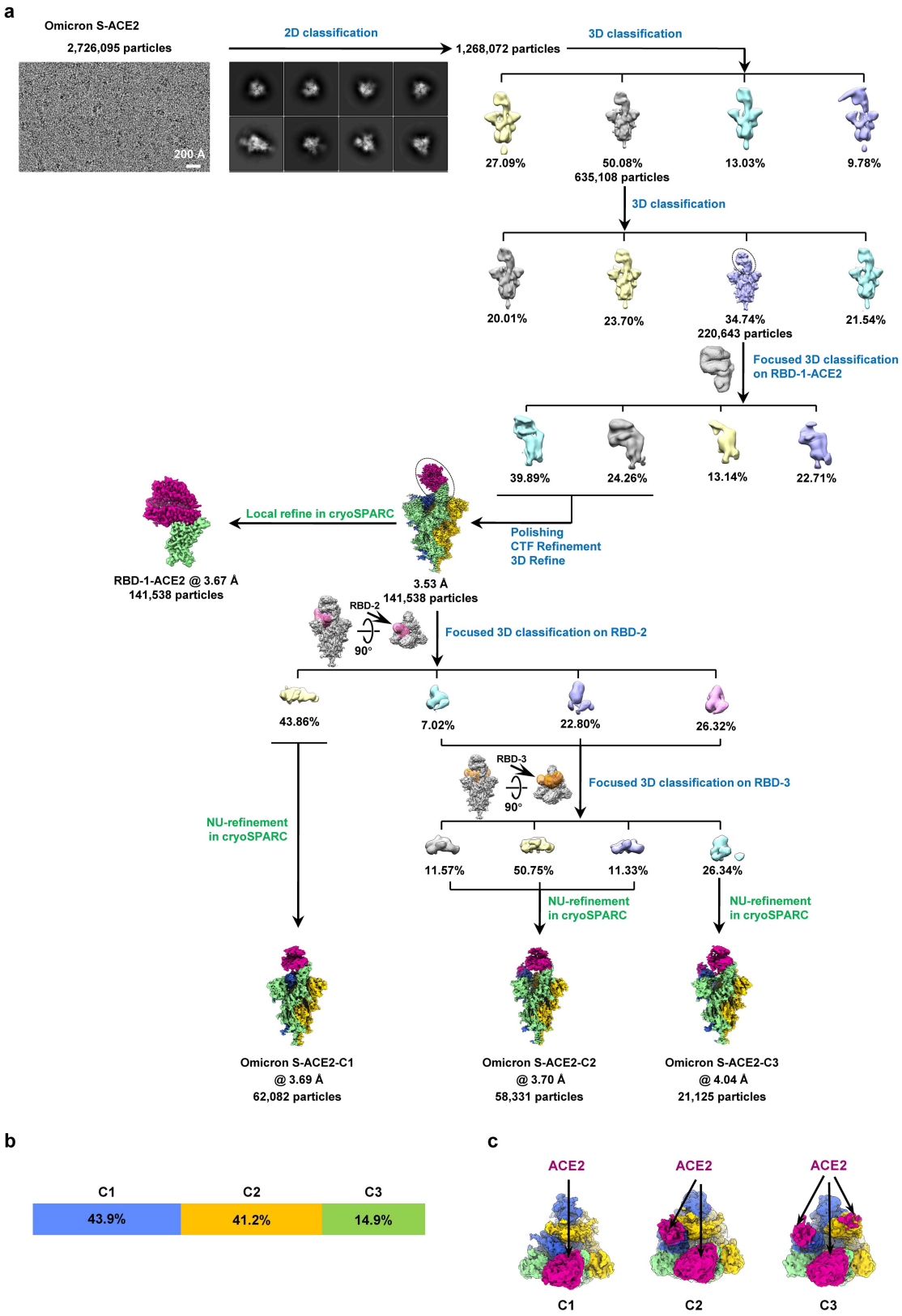

Extended Data Fig. 3 | Cryo-EM data processing procedure for the Omicron S-ACE2 complex. a, Data processing procedure for the Omicron S-ACE2 dataset. A representative original micrograph and the reference-free 2D class averages are also presented. The masks for the focused 3D classification on RBD-2 and RBD-3 regions are shown as pink and orange transparent surfaces, respectively. **b**, Population distribution of the Omicron S-ACE2-C1/-C2/-C3 states. **c**, Lower threshold rendering of the Omicron S-ACE2-C1/-C2/-C3 maps. ACE2 density (violet red) also associates with RBD-2 or RBD-3 in the C2 and C3 states, although appearing weaker than that of the stably associated ACE2 on RBD-1, indicating a dynamic ACE2 association with RBD-2/−3.

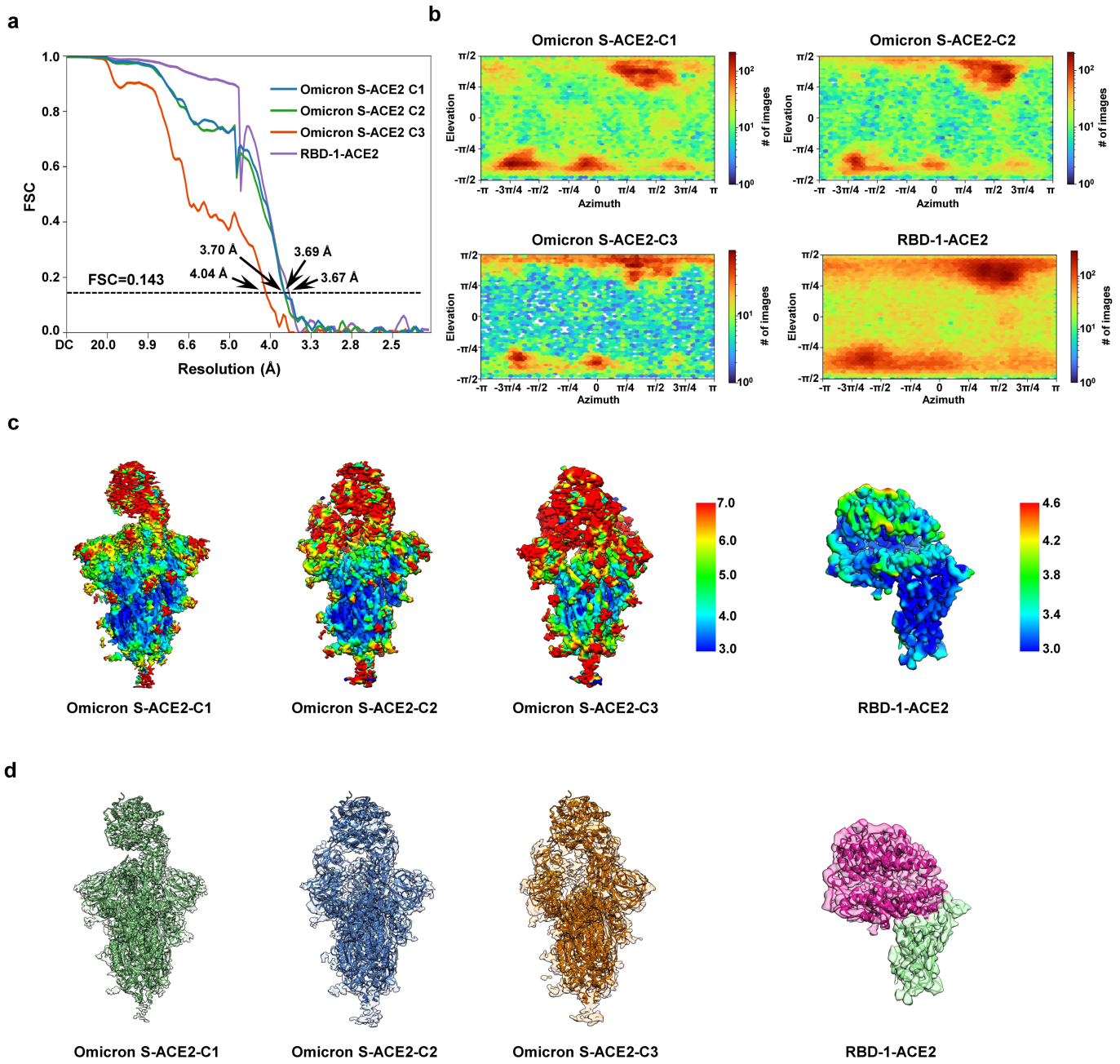

Extended Data Fig. 4 | Cryo-EM analysis on the Omicron S-ACE2 complex. **a**, Resolution assessment of the cryo-EM maps by FSC at 0.143 criterion. **b**, Angular distribution of the Omicron S-ACE2-C1/-C2/-C3 and RBD-1-ACE2 maps. **c, d**, Local resolution evaluation (**c**) and model-map fitting (**d**) for the Omicron S-ACE2 maps and the RBD-1-ACE2 map.

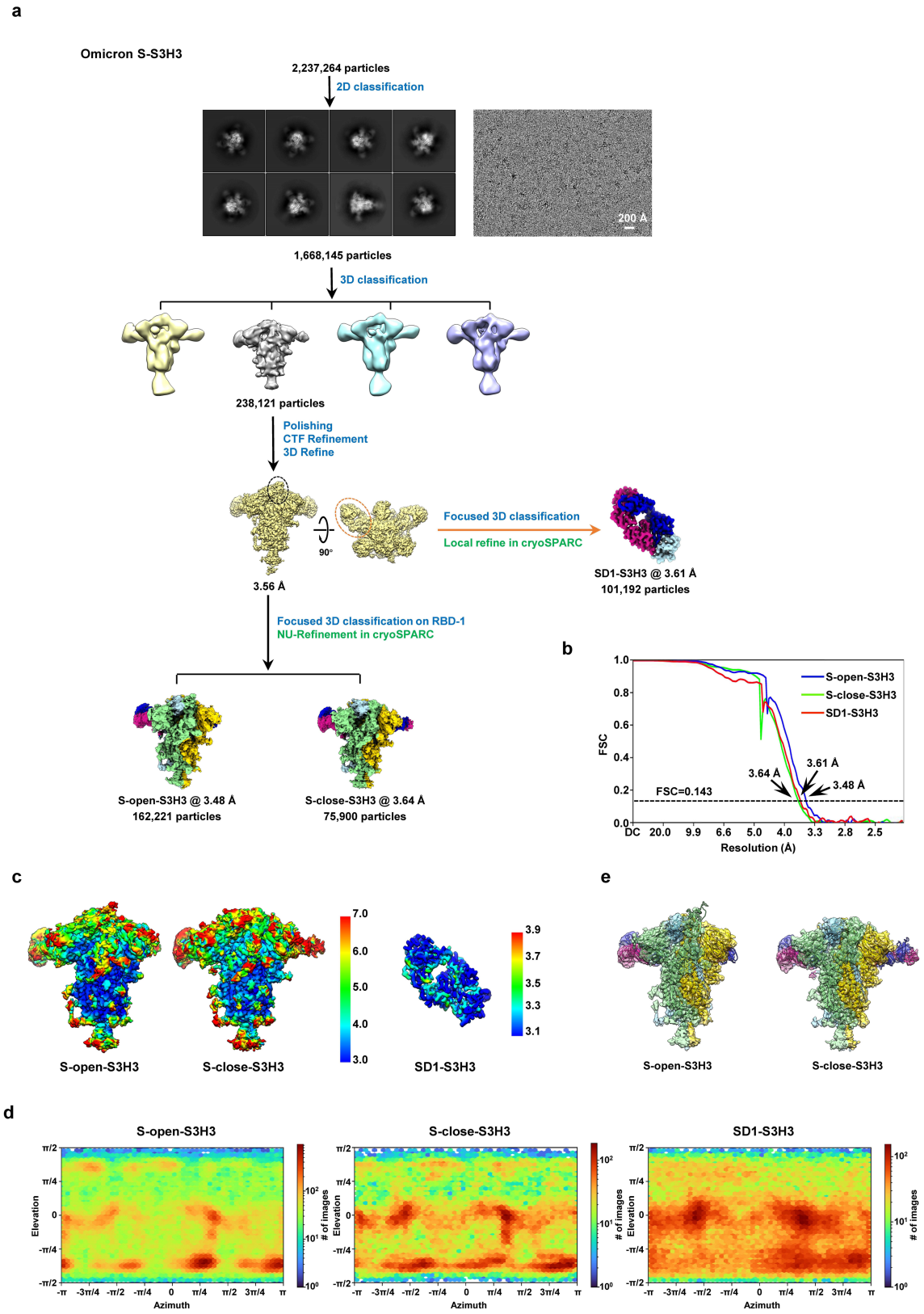

Extended Data Fig. 5 | Cryo-EM analysis on the Omicron S-S3H3 Fab complex. a, Data processing workflow for the Omicron S-S3H3 Fab complex. A representative original micrograph and the reference-free 2D class averages are also presented. **b**, Resolution assessment of the cryo-EM maps by FSC at 0.143 criterion. **c**, Local resolution evaluation of the Omicron S-S3H3 and SD1-S3H3 maps. **d**, Angular distribution for the three Omicron S-S3H3 complexes. **e**, Model-map fitting for the Omicron S-S3H3 complexes.

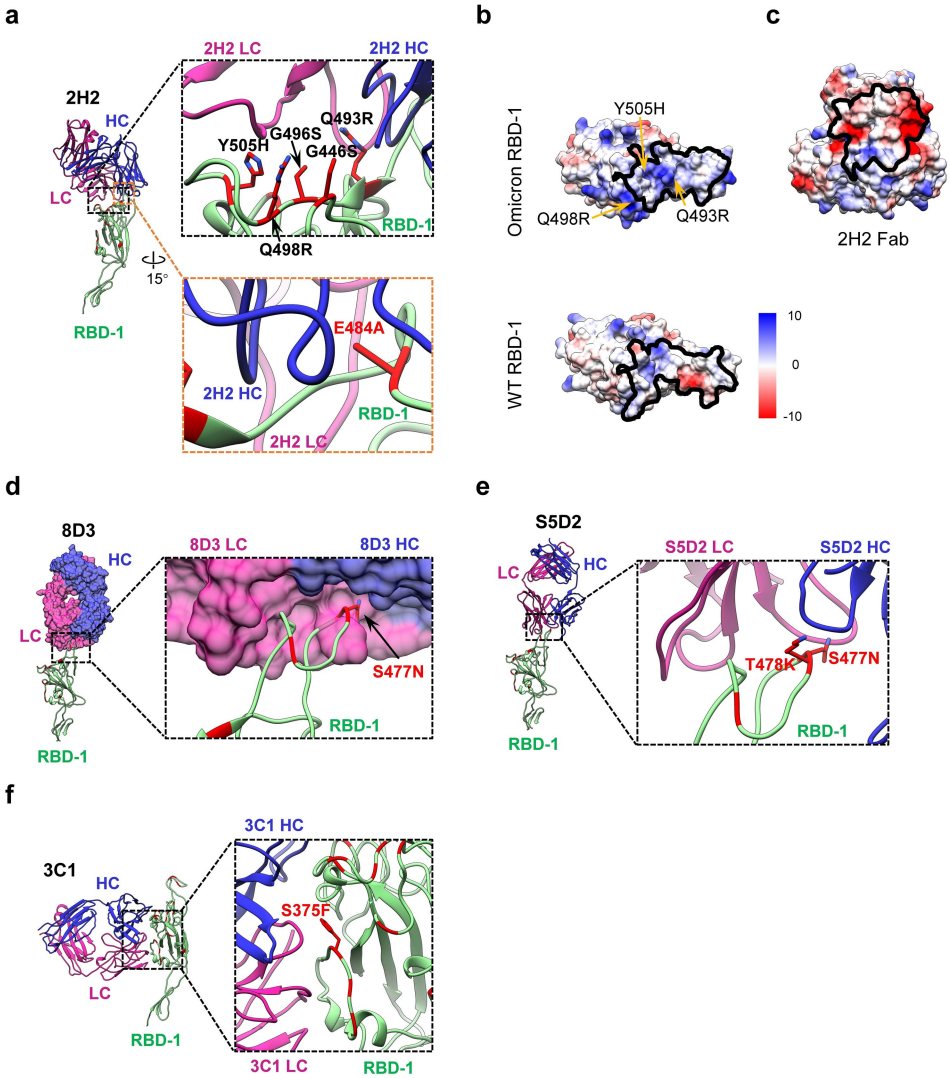

Extended Data Fig. 6 | Structural basis of 2H2 antibody retaining neutralization potency and 8D3/S5D2/3C1 antibodies losing their neutralization potency against Omicron. a, Model of the Omicron RBD-2H2 Fab interaction interface, obtained by docking of the RBD-bound 2H2 (PDB ID: 7DK4) onto the RBD-1 structure from our current Omicron S-open. **b**, The electrostatic surface properties of Omicron and WT RBDs, with the black line depicting the footprint of 2H2 on RBD-1. The residues with substantial electrical charge changes are indicated. **c**, The electrostatic surface property of 2H2 Fab, with the black line depicting the footprint of RBD-1 on 2H2. **d**–**f**, Docking of RBD-bound 8D3/S5D2/3C1 (PDB ID: 7W9F/7WCR/7DCC, respectively) onto the Omicron RBD-1 structure. Residue S477N that may potentially clash with the 8D3 Fab is labeled (**d**). Residues S477N and T478K that may break the H-bond network between RBD and S5D2 Fab are labeled (**e**). Residue S375F that may contribute to the Omicron's escape of 3C1 binding and neutralization is labeled (**f**). All substituted residues in Omicron RBD-1 are colored in red.

Extended Data Table 1 | Cryo-EM data collection and refinement statistics for Omicron S, Omicron S-ACE2, and Omicron S-S3H3

	S-close (EMDB-32556) (PDB 7WK2)	S-open (EMDB-32854) (PDB 7WVN)	S-open-2 (EMDB-32855) (PDB 7WVO)	S-ACE2-C1 (EMDB-32558) (PDB 7WK4)	S-ACE2-C2 (EMDB-32856) (PDB 7WVP)	S-ACE2-C3 (EMDB-32857) (PDB 7WVQ)	RBD-1-ACE2 (EMDB-32560) (PDB 7WK6)	S-open-S3H3 (EMDB-32563) (PDB 7WK9)	S-close-S3H3 (EMDB-32564) (PDB 7WKA)	SD1-S3H3 (EMDB-32562) (PDB 7WK8)
Data collection and processing										
Magnification	64,000									
Voltage (kV)	300									
Electron exposure (e^{-}/Å^2)	50.2									
Defocus range (μm)	-0.8 to -2.5									
Pixel size (Å)	1.093									
Symmetry imposed	C1									
Initial particle images (no.)	761,519	761,519	761,519	2,726,095	2,726,095	2,726,095	2,726,095	2,237,264	2,237,264	2,237,264
Final particle images (no.)	108,509	30,967	38,906	62,082	58,331	21,125	141,538	162,221	75,900	101,192
Map resolution (Å)	3.08	3.40	3.41	3.69	3.70	4.04	3.67	3.48	3.64	3.61
FSC threshold	0.143									
Map resolution range (Å)	2.5-5.0	3.0-6.5	3.0-6.5	3.0-7.0	3.0-7.0	3.0-7.0	3.0-4.6	3.0-7.0	3.0-7.0	3.1-3.9
Refinement										
Initial model used (PDB code)	7W94	7W92	7W92	7W98	7W98	7W98	7W9I	7WDF	7WDF	7WD8
Model resolution (Å)	3.8	4.0	4.0	4.5	4.4	7.8	3.9	4.1	4.2	3.6
FSC threshold	0.5									
Model resolution range (Å)	3.8	4.0	4.0	4.5	4.4	7.8	3.9	4.1	4.2	3.6
Map sharpening *B* factor (Å^2)	-77.8	-59.8	-60.4	-83.8	-90.1	-156.88	-129.7	-108.1	-93.9	-133.3
Model composition										
Non-hydrogen atoms	24,882	24,808	23,191	29,545	29,605	29,531	6,430	29,745	31,353	3,982
Protein residues	3,162	3,162	2,961	3,743	3,750	3,741	791	3,805	4,017	516
Ligands	0	0	0	0	0	0	0	0	0	0
B factors (Å^2)										
Protein	106.21	145.32	129.50	174.20	246.11	251.45	99.00	179.47	183.22	67.06
Ligand	0	0	0	0	0	0	0	0	0	0
R.m.s. deviations										
Bond lengths (Å)	0.006	0.006	0.006	0.005	0.005	0.008	0.008	0.005	0.005	0,005
Bond angles (°)	0.814	0.793	0.794	0.857	0.833	1.027	1.301	1.130	1.145	1.117
Validation										
MolProbity score	1.24	1.20	1.20	1.41	1.41	1.53	1.66	1.38	1.37	1.59
Clashscore	2.15	1.85	1.85	3.87	3.37	3.82	5.57	3.08	3.13	5.60
Poor rotamers (%)	0.14	0.07	0.04	0.49	0.27	0.46	0.57	0.36	0.23	0.22
Ramachandran plot										
Favored (%)	96.22	96.24	96.29	96.40	95.97	94.71	94.92	95.95	96.14	95.87
Allowed (%)	3.78	3.73	3.68	3.44	3.95	5.13	4.70	3.89	3.74	3.94
Disallowed (%)	0.00	0.03	0.03	0.16	0.08	0.16	0.38	0.16	0.13	0.20

Extended Data Table 2 | Omicron S-close protomer 1/2 and protomer 1/3 interactions

S-close Protomer 1		S-close Protomer 2		Interaction	Distance (Å)
Residue	Atom	Residue	Atom		
PHE 43	[O]	ARG 567	[N]	H-bond	3.29
PRO 230	[O]	ARG 357	[OH]	H-bond	3.68
TYR 369	[OH]	ASN 460	[NH1]	H-bond	3.03
ASN 370	[OD1]	TYR 421	[ND2]	H-bond	2.39
ALA 372	[O]	ASN 417	[OH]	H-bond	3.02
PHE 375	[O]	ARG 408	[NH1]	H-bond	3.01
ASP 737	[OD1]	ASN 317	[NH2]	H-bond	2.86
THR 739	[OG1]	ARG 319	[NH2]	H-bond	3.01
GLN 755	[O]	LYS 969	[N]	H-bond	3.20
GLN 755	[O]	SER 968	[OG]	H-bond	2.40
GLN 755	[O]	PHE 970	[N]	H-bond	3.59
SER 758	[OG]	GLN 965	[NE2]	H-bond	2.47
ILE 788	[O]	ASN 703	[N]	H-bond	3.20
PRO 863	[O]	ALA 668	[N]	H-bond	2.87
LEU 864	[O]	GLY 669	[N]	H-bond	2.93
SER 884	[OG]	TYR 707	[N]	H-bond	2.40
GLN 895	[O]	ALA 713	[OH]	H-bond	3.51
PHE 981	[O]	LYS 386	[OH]	H-bond	2.47
ARG 983	[O]	SER 383	[N]	H-bond	2.94
LEU 984	[O]	LYS 386	[NZ]	H-bond	3.47
GLU 1031	[OE2]	VAL 1040	[N]	H-bond	3.50
GLU 1111	[OE2]	SER 1123	[N]	H-bond	3.31
TYR 200	[OH]	GLU 516	[O]	H-bond	2.57
TYR 369	[OH]	ASN 460	[OE2]	H-bond	3.09
ALA 372	[N]	ASN 417	[OD1]	H-bond	3.62
GLN 762	[NE2]	THR 961	[OG]	H-bond	3.07
LYS 764	[NZ]	GLN 314	[OE1]	H-bond	3.00
THR 768	[OG1]	GLN 314	[OE1]	H-bond	3.49
GLN 787	[NE2]	ALA 701	[O]	H-bond	2.76
ILE 788	[N]	ALA 701	[O]	H-bond	3.41
LYS 790	[N]	ASN 703	[OE2]	H-bond	3.87
LYS 790	[NZ]	GLU 702	[OG1]	H-bond	2.70
LYS 856	[NZ]	THR 572	[O]	H-bond	3.88
GLN 895	[NE2]	ALA 706	[OD2]	H-bond	2.77
TYR 904	[OH]	GLY 1093	[O]	H-bond	2.41
SER 975	[OG]	ASP 571	[OE2]	H-bond	3.72
ASN 978	[ND2]	LYS 547	[OE1]	H-bond	3.23
LYS 790	[NZ]	GLU 702	[OE1]	Salt bridge	3.91
LYS 790	[NZ]	GLU 702	[OE2]	Salt bridge	2.70

S-close Protomer 1		S-close Protomer 3		Interaction	Distance (Å)
Residue	Atom	Residue	Atom		
GLU 516	[OE1]	TYR 200	[OH]	H-bond	2.99
ASN 417	[OD1]	ALA 372	[N]	H-bond	2.60
GLN 314	[O]	LYS 764	[NZ]	H-bond	3.84
ALA 701	[O]	GLN 787	[NE2]	H-bond	3.00
ALA 701	[O]	ILE 788	[N]	H-bond	3.25
ASN 703	[O]	LYS 790	[N]	H-bond	3.84
GLU 702	[OE2]	LYS 790	[NZ]	H-bond	2.47
SER 698	[O]	TYR 873	[OH]	H-bond	3.53
TYR 707	[OH]	THR 883	[OG1]	H-bond	3.08
TYR 707	[OH]	SER 884	[OG]	H-bond	3.50
ALA 706	[O]	GLN 895	[NE2]	H-bond	3.00
LYS 547	[O]	ASN 978	[ND2]	H-bond	3.20
ARG 567	[N]	PHE 43	[O]	H-bond	3.83
LYS 557	[NZ]	SER 45	[OG]	H-bond	3.42
ASN 417	[ND2]	ALA 372	[O]	H-bond	2.66
ARG 408	[NH2]	PHE 375	[O]	H-bond	3.30
ARG 408	[NH2]	THR 376	[OG1]	H-bond	2.44
ASN 317	[ND2]	ASP 737	[OD2]	H-bond	2.33
ARG 319	[NH2]	ASP 737	[OD2]	H-bond	3.79
ARG 319	[NH1]	ASP 745	[OD1]	H-bond	3.68
LYS 969	[N]	GLN 755	[O]	H-bond	2.86
PHE 970	[N]	GLN 755	[O]	H-bond	3.12
GLN 965	[NE2]	SER 758	[OG]	H-bond	2.46
ALA 701	[N]	LYS 786	[O]	H-bond	3.67
ASN 703	[N]	ILE 788	[O]	H-bond	3.23
ALA 668	[N]	PRO 863	[O]	H-bond	2.96
GLY 669	[N]	LEU 864	[O]	H-bond	3.54
ALA 713	[N]	GLN 895	[O]	H-bond	3.38
LYS 386	[NZ]	PHE 981	[O]	H-bond	2.50
SER 383	[N]	ARG 983	[O]	H-bond	3.20
LYS 386	[NZ]	LEU 984	[O]	H-bond	2.68
VAL1040	[N]	GLU1031	[OE2]	H-bond	3.82
SER1123	[OG]	GLU1111	[OE2]	H-bond	2.98
GLU 702	[OE2]	LYS 790	[NZ]	Salt bridge	2.47
ARG 319	[NH2]	ASP 737	[OD2]	Salt bridge	3.79
ARG 319	[NH1]	ASP 745	[OD1]	Salt bridge	3.68

Extended Data Table 3 | Interaction interface analysis (upper table) and footprint distance measurement (lower table) for Omicron RBD-1-ACE2 structure

Omicron S RBD-1		ACE2		Interaction	Distance(Å)
Residue	Atom	Residue	Atom		
ASN 487	[OD1]	TYR 83	[OH]	H-bond	2.45
TYR 489	[OH]	TYR 83	[OH]	H-bond	3.00
SER 494	[O]	HIS 34	[NE2]	H-bond	3.09
SER 496	[O]	LYS 353	[NZ]	H-bond	3.65
SER 496	[OG]	LYS 353	[NZ]	H-bond	2.82
ASN 477	[ND2]	SER 19	[O]	H-bond	3.86
ASN 477	[ND2]	SER 19	[OG]	H-bond	3.38
ASN 487	[ND2]	GLN 24	[OE1]	H-bond	2.74
ARG 493	[NH2]	GLU 35	[OE1]	H-bond	3.58
TYR 449	[OH]	ASP 38	[OD1]	H-bond	2.79
ARG 498	[NH1]	ASP 38	[OD1]	H-bond	3.37
TYR 449	[OH]	ASP 38	[OD2]	H-bond	2.62
TYR 449	[OH]	GLN 42	[OE1]	H-bond	3.27
ARG 498	[NH1]	GLN 42	[OE1]	H-bond	3.04
HIS 505	[ND1]	LYS 353	[O]	H-bond	2.85
THR 500	[OG1]	ASP 355	[OD2]	H-bond	3.40
ARG 493	[NH2]	GLU 35	[OE1]	Salt bridge	3.58
ARG 493	[NH2]	GLU 35	[OE2]	Salt bridge	3.93
ARG 498	[NH1]	ASP 38	[OD1]	Salt bridge	3.37

Omicron S RBD-1	ACE2
Y449	D38, Q42
Y453	H34
L455	D30
F456	T27, D30, K31
A475	Q24, T27
N477	S19
F486	M82, Y83
N487	Q24, Y83
Y489	T27, F28
R493	H34, E35
S494	H34
S496	D38, K353
R498	D38, Y41, Q42
T500	Y41, D355, R357
Y501	Y41, K353, G354, D355
G502	G354
H505	K353, G354

Extended Data Table 4 | Interaction interface analysis (upper table) and footprint distance measurement (lower table) for Omicron SD1-S3H3 structure

Omicron S		S3H3		Interaction	Distance(Å)
Residue	Atom	Residue	Atom		
LYS 537	[NZ]	ASP 55	[OD2]	H-bond	3.35
THR 581	[OG1]	ASP 102	[OD1]	H-bond	3.25
SER 555	[O]	SER 32	[OG]	H-bond	3.05
ILE 584	[O]	SER 32	[OG]	H-bond	3.80
LYS 537	[NZ]	ASP 55	[OD2]	Salt bridge	3.35

Omicron S	S3H3
T323	S54
E324	R31
N532	F32
L533	Y101
V534	R31, W33
K535	Y101
N536	W33, R59, L98
K537	H52, D55
E554	Y36, S95, R96
S555	A31, S32
N556	A31, R96
T581	D102
L582	Y34
E583	Y103
I584	S32

Heavy chain
Light chain

nature portfolio

Corresponding author(s): Yao Cong

Last updated by author(s): Jan 24, 2022

Reporting Summary

Nature Portfolio wishes to improve the reproducibility of the work that we publish. This form provides structure for consistency and transparency in reporting. For further information on Nature Portfolio policies, see our Editorial Policies and the Editorial Policy Checklist.

Statistics

For all statistical analyses, confirm that the following items are present in the figure legend, table legend, main text, or Methods section.

n/a	Confirmed	
☐	☒	The exact sample size (*n*) for each experimental group/condition, given as a discrete number and unit of measurement
☐	☒	A statement on whether measurements were taken from distinct samples or whether the same sample was measured repeatedly
☒	☐	The statistical test(s) used AND whether they are one- or two-sided *Only common tests should be described solely by name; describe more complex techniques in the Methods section.*
☒	☐	A description of all covariates tested
☒	☐	A description of any assumptions or corrections, such as tests of normality and adjustment for multiple comparisons
☐	☒	A full description of the statistical parameters including central tendency (e.g. means) or other basic estimates (e.g. regression coefficient) AND variation (e.g. standard deviation) or associated estimates of uncertainty (e.g. confidence intervals)
☒	☐	For null hypothesis testing, the test statistic (e.g. *F*, *t*, *r*) with confidence intervals, effect sizes, degrees of freedom and *P* value noted *Give P values as exact values whenever suitable.*
☒	☐	For Bayesian analysis, information on the choice of priors and Markov chain Monte Carlo settings
☒	☐	For hierarchical and complex designs, identification of the appropriate level for tests and full reporting of outcomes
☒	☐	Estimates of effect sizes (e.g. Cohen's *d*, Pearson's *r*), indicating how they were calculated

Our web collection on statistics for biologists contains articles on many of the points above.

Software and code

Policy information about availability of computer code

Data collection	FEI TEM user interface, EPU 2.11
Data analysis	Octet Data Analysis 11.0, GraphPad Prism (version 8), MotionCor2, RELION 3.1, CTFFIND 4.1.8, Phenix 1.19.2-4158, Rosetta 2017, COOT 0.9.6.2-pre, UCSF Chimera 1.15, UCSF ChimeraX 1.3, PDBePISA, cryoSPARC v3.3.1, deepEMhancer

For manuscripts utilizing custom algorithms or software that are central to the research but not yet described in published literature, software must be made available to editors and reviewers. We strongly encourage code deposition in a community repository (e.g. GitHub). See the Nature Portfolio guidelines for submitting code & software for further information.

Data

Policy information about availability of data

All manuscripts must include a data availability statement. This statement should provide the following information, where applicable:

- Accession codes, unique identifiers, or web links for publicly available datasets
- A description of any restrictions on data availability
- For clinical datasets or third party data, please ensure that the statement adheres to our policy

All data presented in this study are available within the figures and in the Supplementary Information. For the SARS-CoV-2 Omicron variant, related cryo-EM maps have been deposited at the Electron Microscopy Data Bank with accession codes EMD-32556 [https://www.ebi.ac.uk/pdbe/entry/emdb/EMD-32556], EMD-32557 [https://www.ebi.ac.uk/pdbe/entry/emdb/EMD-32557], EMD-32558 [https://www.ebi.ac.uk/pdbe/entry/emdb/EMD-32558], EMD-32559 [https://www.ebi.ac.uk/pdbe/entry/emdb/EMD-32559], EMD-32560 [https://www.ebi.ac.uk/pdbe/entry/emdb/EMD-32560], EMD-32562 [https://www.ebi.ac.uk/pdbe/entry/emdb/EMD-32562], EMD-32563 [https://www.ebi.ac.uk/pdbe/entry/emdb/EMD-32563], and EMD-32564 [https://www.ebi.ac.uk/pdbe/entry/emdb/EMD-32564], and associated atomic models have been deposited in the Protein Data Bank with accession codes 7WK2 [https://doi.org/10.2210/pdb7WK2/pdb], 7WK3 [https://

doi.org/10.2210/pdb7WK3/pdb], 7WK4 [https://doi.org/10.2210/pdb7WK4/pdb], 7WK5 [https://doi.org/10.2210/pdb7WK5/pdb], 7WK6 [https://doi.org/10.2210/pdb7WK6/pdb], 7WK8 [https://doi.org/10.2210/pdb7WK8/pdb], 7WK9 [https://doi.org/10.2210/pdb7WK9/pdb], and 7WKA [https://doi.org/10.2210/pdb7WKA/pdb] for S-close, S-open, S-ACE2-C1, S-ACE2-C2, RBD-1-ACE2, SD1-S3H3, S-open-S3H3 and S-close-S3H3, respectively.

Field-specific reporting

Please select the one below that is the best fit for your research. If you are not sure, read the appropriate sections before making your selection.

☒ Life sciences ☐ Behavioural & social sciences ☐ Ecological, evolutionary & environmental sciences

For a reference copy of the document with all sections, see nature.com/documents/nr-reporting-summary-flat.pdf

Life sciences study design

All studies must disclose on these points even when the disclosure is negative.

Sample size	No statistical methods were used to determine sample size for EM data. Sample sizes were determined based on the ability to get sufficient particles for 3D reconstruction and particles with good features are selected.
Data exclusions	The cryo-EM images of poor quality were deleted based on the defocus, astigmatism and reslution for better resolution.
Replication	Experimental findings were reliably reproduced. Most of the experiments were replicated two or three times.
Randomization	Randomization was not relevant for this study, as data were collected automatically and there were no samples allocated into control and experimental groups.
Blinding	Blinding was not relevant for this study, as data were collected automatically, and the data under investigation need to be known.

Reporting for specific materials, systems and methods

We require information from authors about some types of materials, experimental systems and methods used in many studies. Here, indicate whether each material, system or method listed is relevant to your study. If you are not sure if a list item applies to your research, read the appropriate section before selecting a response.

Materials & experimental systems

n/a	Involved in the study
☐	☒ Antibodies
☐	☒ Eukaryotic cell lines
☒	☐ Palaeontology and archaeology
☒	☐ Animals and other organisms
☒	☐ Human research participants
☒	☐ Clinical data
☒	☐ Dual use research of concern

Methods

n/a	Involved in the study
☒	☐ ChIP-seq
☒	☐ Flow cytometry
☒	☐ MRI-based neuroimaging

Antibodies

Antibodies used	HRP-conjugated anti-mouse IgG (Sigma, A0168-1ML); anti-WT-Spike-protein MAbs 3C1, 2H2, 8D3, S5D2, and S3H3 (50 ng/well [1 μg/mL] for each MAb in ELISA) were prepared in Zhong Huang's lab.
Validation	The specifications of commercially available HRP-conjugated anti-mouse IgG can be found on the manufacture's website (https://www.sigmaaldrich.com/HK/zh/product/sigma/a0168). Anti-WT-Spike-protein MAbs 2H2, 3C1, and 8D3 (Zhang et al. Nature communications. 2021, 12, 264; https://doi.org/10.1038/s41467-020-20465-w), and S5D2 and S3H3 (Xu et al., 2021, Emerging Microbes & Infections. https://doi.org/10.1080/22221751.2021.2024455) have been validated previously.

Eukaryotic cell lines

Policy information about cell lines

Cell line source(s)	Human ACE2-expressing HEK 293T cells (293T-hACE2) were generated in Zhong Huang's lab; HEK293F suspension cells, Thermo fisher.
Authentication	293T-hACE2 cells have been validated previously (Zhang et al. Nature communications. 2021, 12, 264; https://doi.org/10.1038/s41467-020-20465-w). HEK293F cells were not authenticated further after purchase.

Mycoplasma contamination	Cell lines have not recently been tested for Mycoplasma contamination.
Commonly misidentified lines (See ICLAC register)	No commonly misidentified lines were used.